Fragment velocities, energies, and masses from fast neutron induced fission of ^{235}U

R. Müller*
Universität Tübingen, Physikalisches Institut, Tübingen, Federal Republic of Germany

A. A. Naqvi,† F. Käppeler, and F. Dickmann
Kernforschungszentrum Karlsruhe GmbH, Institut für Angewandte Kernphysik, D-7500 Karlsruhe, Federal Republic of Germany

(Received 10 June 1982; revised manuscript received 30 November 1982)

We report on a complete $(2E,2v)$ experiment for fast neutron induced fission on ^{235}U. The energy dependence of fragment properties so far known only for thermal neutron induced fission is studied. Experimental problems as well as difficulties in data analysis are considered in detail in order to obtain clean and unbiased results. In particular, a self-consistent determination of the fragment total kinetic energy ($E_{K,\mathrm{tot}}$) was achieved by comparing the results obtained via the respective velocities and pulse heights. We find systematic discrepancies of 2 MeV if $E_{K,\mathrm{tot}}$ is determined from the observed pulse heights with the calibration scheme of Schmitt *et al.* Therefore, refined calibration constants were deduced by comparison with accurate radiochemical mass yields. Measurements were performed at neutron energies of 0.50 and 5.55 MeV. Our results include mean values of fragment properties before and after neutron evaporation, e.g., of fragment velocities and masses, total kinetic energies, and the respective variances. We also show the distributions of fragment mass, of $E_{K,\mathrm{tot}}$, and of the variance of $E_{K,\mathrm{tot}}$. In addition, the number of prompt fission neutrons ν is given as a function of fragment mass. Our resolution of 2.1 mass units reveals fine structure not only in the fragment mass distribution but also in $E_{K,\mathrm{tot}}(A^*)$ and $\nu(A^*)$. For the lower neutron energy of 0.50 MeV the present results compare reasonably well with similar measurements performed with thermal neutrons. Apparently the 0.5 MeV increase in saddle point excitation does not alter the results significantly. The improved accuracy of this measurement is demonstrated by comparison of our neutron emission data with direct measurements of fission neutrons. At the higher neutron energy of 5.55 MeV we observe the expected decrease of shell and pairing effects which indicates an increase in nuclear temperature. These results are in qualitative agreement with the model of Wilkins, Chasman, and Steinberg. However, a striking discrepancy exists for the number of fission neutrons, where we find that the increase in the total number of fission neutrons is totally accounted for by heavy fragments alone.

I. INTRODUCTION

Nuclear fission has been a longstanding theme of scientific investigations. Since the rise of heavy ion physics the common features of the two fields have been emphasized, especially the problem of large scale nuclear collective motion. However, fission is distinct from other heavy ion reactions involving comparable masses in that the fissioning nucleus can be prepared in saddle points with little or no excitation energy. From such points in the space of deformation parameters the system is free to either coalesce to a compound nucleus or to separate into fission fragments. For small excitation energy the resonances above the saddle point are narrow. One can distinguish collective and particle states and ask how they develop as the deformation proceeds from saddle to scission. Since the deformation energy has a maximum at the saddle point with respect to the fission mode, more and more energy becomes available for collective and internal excitation as the nucleus proceeds towards scission. Hence fission dynamics will tend to mix the low lying saddle point states with each other and with other modes. Beyond the scission point the polarizing Coulomb force between the nascent fragments is transformed into kinetic energy of the fragment centers. The fission fragments dispose of their deformation and excitation energy by neutron and gamma emission before entering the detection system. Therefore multiparameter precision experiments have to be performed to collect a maximum of information about a single fission event. Quantities of special interest are the following:

odd-even effects in the mass and charge distribution which permit conclusions on the persistence of pair correlations in the fission process;

neutron- and gamma-ray emission from fragments of given mass and charge which allow for estimates on the influence of fragment shell-structure in the scission configuration (both ground state shells and deformed shells can be shown to be important);

the influence of the excitation energy of the fissioning nucleus on the above-mentioned quantities in order to observe how rapidly specific quantum effects vanish as a function of energy.

In the following we present results of a four parameter experiment on neutron induced fission of ^{235}U for neutron

energies of 0.50 and 5.55 MeV corresponding to saddle point excitation energies of 1.3 and 6.3 MeV in the fissioning compound system ^{236}U. The four measured quantities are the velocities and kinetic energies of two corresponding fission fragments. The experiment is described in Sec. II and the data analysis discussed in Sec. III. In Sec. IV the results are given and in Sec. V a comparison with models of nuclear fission is presented.

II. EXPERIMENT

A. Principle

At the scission point the fissioning nucleus of mass A_c separates into two fragments $A^*_{1,2}$ which are emitted under 180 deg with velocities $v^*_{1,2}$. In the following an asterisk (*) denotes primary quantities before neutron evaporation. Momentum and mass conservation yield the relations between $A^*_{1,2}$ and $v^*_{1,2}$, which in turn yield the kinetic energies $E^*_{1,2}$ and the total kinetic energy $E^*_{K,\mathrm{tot}}$,

$$A^*_{1,2}=\frac{v^*_{2,1}}{v^*_1+v^*_2}A_c \ , \tag{1}$$

$$E^*_{1,2}=\frac{A^*_{1,2}}{2}v^{*2}_{1,2} \ , \tag{2}$$

$$E^*_{K,\mathrm{tot}}=E^*_1+E^*_2=\frac{A_c}{2}v^*_1v^*_2 \ . \tag{3}$$

The primary velocities $v^*_{1,2}$ cannot be measured because the fragments evaporate neutrons within $\lesssim 10^{-14}$ s. However, if one assumes that the neutrons are emitted from fully accelerated fragments with forward/backward symmetry ($\overline{\cos\theta}=0$), then on an average there is no change of velocity: $v^*_i=v_i$. Obviously, the resolution in those quantities which are calculated from the secondary velocities $v_{1,2}$, such as $v^*_{1,2}$, $A^*_{1,2}$, and $E^*_{1,2}$, is limited by the neutron emission itself.

The fragment masses after neutron emission can be calculated immediately from the measured kinetic energies

$$A_{1,2}=\frac{2E_{1,2}}{v^2_{1,2}} \ . \tag{4}$$

The number of neutrons emitted as a function of fragment mass follows then as

$$\bar{\nu}(A^*_{1,2})=\frac{A^*_{1,2}-A_{1,2}}{m_{\mathrm{n}}} \ , \tag{5}$$

with m_{n} being the neutron mass. Equations (1)—(5) show the kinds of physical information that can be deduced from the kinetic energies and velocities of correlated fragments.

Up to now only one complete $(2E,2v)$ experiment has been carried out with thermal neutrons, by Andritsopoulos,[1] with flight paths of about 1.7 m which were required by the limited time resolution of 3.5 ns. The rather long flight path has the disadvantage that the observed ensemble of fission events is not necessarily the original one because the colinearity of the fragment direction is disturbed by neutron emission. This effect is enhanced by additional straggling in the foil of the time zero detector for the time-of-flight measurement.

It was the aim of this work to perform a $(2E,2v)$ experiment by which the entire neutron energy range up to the threshold of (n,n′f) reactions could be investigated. (Beyond this threshold the compound system is no longer defined.) The use of short flight paths (<40 cm) is important for the physical reason that one wants to observe an unbiased ensemble of events and for the technical reason that one must achieve an optimum solid angle for compensation of the rather weak neutron flux available for MeV neutrons from an accelerator. In order to maintain the experimental resolution the reduction in flight path had to be compensated by improved time resolution. In addition to good time resolution two other very important features should be pointed out explicitly:

(a) As is obvious from Eqs. (1)—(5), the velocity determination is the crucial point of the experiment. An accurate velocity determination requires at least two measurements, one with a short and another with a long flight path in order to eliminate the different electronic delay for the start and the stop signals as well as the influence of fragment specific properties like mass or kinetic energy on the timing of the detectors.
(b) $\bar{\nu}$ is calculated from the difference of primary and secondary fragment masses. As $\bar{\nu}$ is only about 1% of these masses, it is essential that the mean masses are determined to 0.1% or better. Therefore, the experiment should contain internal calibrations and must be conducted with the greatest care to provide sufficient stability against short and long term variations of important parameters.

B. Mechanical setup

The experimental setup is shown schematically in Fig. 1. The pulsed proton beam of the Karlsruhe 3 MV Van de Graaff accelerator (5 MHz repetition rate, $\lesssim$800 ps pulse width) was used for neutron production. Beam pickup signals served as time marks for the time-of-flight (TOF) measurement and for continuous computer control of the pulse width. With the ^{7}Li(p,n) reaction a neutron spectrum of 500 ± 80 keV was generated, whereas the ^{2}H(d,n) reaction was applied to obtain neutrons of 5550 ± 250 keV energy.

The design of the neutron target and its arrangement relative to the fissile sample was optimized with respect to solid angle and neutron flight path differences. The distance between target and sample is only 15 mm, resulting in an effective solid angle of 0.4 sr. The sample is rectangular (10×14 mm), with the narrow side close to the target. This geometry ensured that differences in neutron flight time were smaller than the pulse width of the accelerator. Since the total interaction time of the neutron burst with the sample was well below 1 ns, it was possible to forego a time zero detector and to use instead the beam pickup signals directly for the fragment velocity determination. The inset in Fig. 1 illustrates the convective target cooling via the 0.5 mm thick copper backing. All parts were as thin as possible to reduce neutron scattering

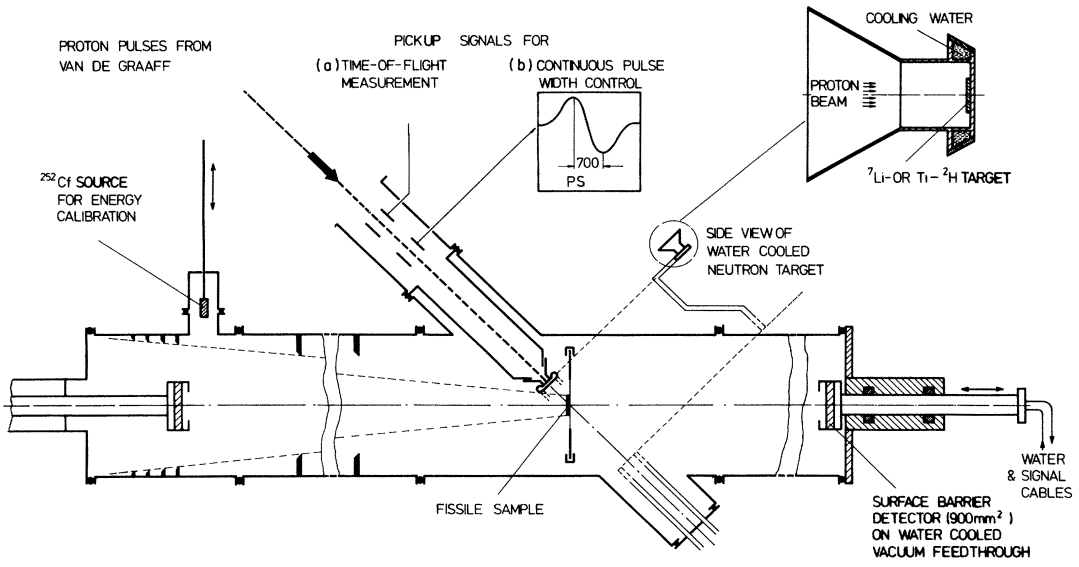

FIG. 1. Schematic sketch of the experimental setup.

to an almost negligible level. The conical connection towards the accelerator guarantees reliable adjustment of the target and shields the fragment detectors against scattered protons.

Various diaphragms in the flight tubes shielded the detectors from scattered fragments. The flight tubes were identical except that one of them could be bent by means of flexible bellows to compensate for the momentum transfer of the incoming neutron. The corresponding deviation from colinearity in the fragment directions was 1.8 deg at 5.55 MeV neutron energy.

The flight tubes were equipped with ^{252}Cf sources which could be inserted into the flight tubes for regular energy calibration at a distance of 10.5 cm from the detectors. The system was evacuated to 1 mPa and the vacuum had to be broken only to change the neutron targets.

C. Fission sources

The samples were layers of 100 μg/cm^2 UO_2 evaporated on 30 μg/cm^2 thick carbon backings. The sample material was enriched in ^{235}U to 99.5% (^{234}U: 0.168%; ^{236}U: 0.027%; ^{238}U: 0.300%) in order to avoid events from fission of ^{238}U at the higher neutron energy of 5.55 MeV. Positioning of the samples was achieved by an exact guide.

D. Detectors

The fission fragment detectors were silicon surface barrier detectors (Ortec AF-90-900-60) with a sensitive area of 33 mm in diameter. Three such detectors (368, 436, and 675 Ω) were used in the course of the measurement. The detectors were mounted in a coaxial fixture which allowed for reflexion-free pulse transfer to the signal cable. As is indicated in Fig. 1, water cooling served for stable operation and for reduction of the reverse current. The detector bias of 100 V was carefully checked and maintained to ±0.5 V throughout the experiment in order to avoid gain drifts. The entire detector mounting was designed as a precisely adjustable vacuum feedthrough, thus allowing for quick and reproducible changes of the fragment flight paths. The ^{252}Cf pulse height distribution was used to ensure that the detectors met the quality specifications given by Schmitt and Pleasonton.[2] One of the detectors had to be replaced when its peak-to-valley ratio in the ^{252}Cf spectrum decreased to a value of 2.7 from radiation damage.

E. Electronics

The main part of the electronics consisted of only a few modules, as can be seen from the block diagram of Fig. 2. The signals from the solid state detectors were split and a sharply differentiated fraction was fed to a fast amplifier via a 470 pF capacitor. This four stage, 50 Ω amplifier had a gain of 150. In between the second and third stages a 10 MHz filter of high Q value was used to suppress the bunching frequency background from the accelerator pulsing system by a factor 35. The subsequent constant fraction discriminator produced the start signal for the time-to-amplitude converter (TAC). The corresponding stop signal was derived from the pulsed accelerator beam by cylindrical pickup electrodes. The TAC output (100 ns conversion range) was then fed to a 8192 channel analog-to-digital converter (ADC). The second fraction of the signals was integrated by a 120 Ω resistor and provides the pulse height information. After shaping and amplification in a charge sensitive preamplifier and a spectroscopy amplifier the pulse height signals were analyzed in 1024 channels.

This main part of the electronics was complemented by two circuits for the calibration of the TAC and for suppression of spurious pulses. The time calibration was achieved by a precise time calibrator module (ORTEC 462) which produced start and stop signals in 10 ns steps over an interval of 160 ns. These signals could be coupled to the TAC by OR gates which were used as switches. In-

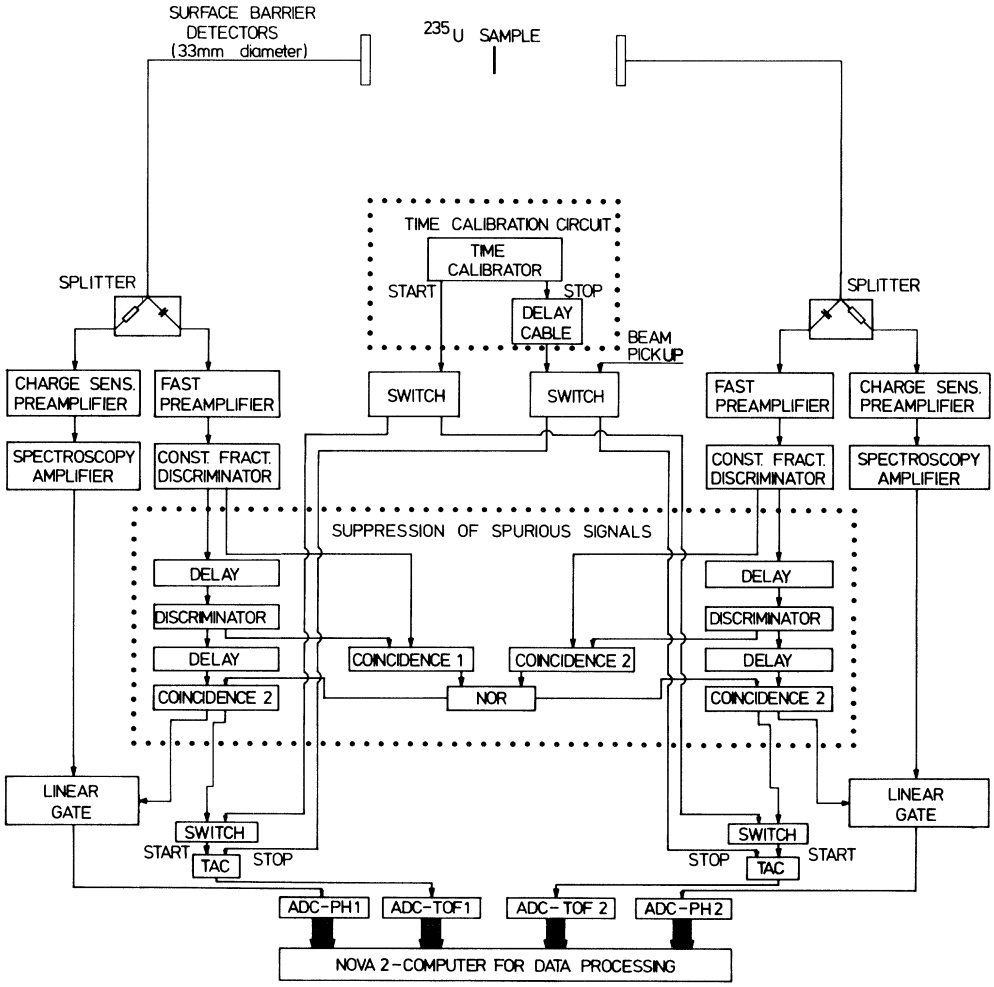

FIG. 2. Block diagram of the electronics. The dashed boxes contain equipment for calibration measurements and for background suppression.

sertion of additional specific delays in the stop circuit yielded even better sensitivity of the calibration procedure.

In the fast branch of the electronics spurious oscillating pulse trains of typically 100 ns duration and a period of ~ 10 ns caused a severe background. These pulses were effectively suppressed by the pileup branch indicated in Fig. 2. Signals were rejected if they were longer than 40 ns and if they followed each other by less than 1 μs.

F. Data accumulation

A special program was developed for accumulating the data in a NOVA2 computer. It was designed for operation in two different modes: measurement or calibration. During the measurements, data were stored in list mode in buffer regions and were then sequentially transferred onto magnetic tape for later analysis. Simultaneously various control spectra were generated which allowed continuous checking. Besides the normal time-of-flight and pulse height spectra for control of detector resolution, two-dimensional spectra, e.g., t_1 vs t_2, were created. These spectra gave a convenient survey of background conditions. In the calibration mode, the ^{252}Cf pulse height spectra and the respective spectra for the time calibration were accumulated for both detectors and subsequently stored on a magnetic disk.

G. Calibration measurements

To reduce the influence of drifts in the electronics or in the detectors, time and energy scales were calibrated daily: The pulse height spectra of the ^{252}Cf sources which were installed in the flight tubes were used to define an energy scale for the fission fragments (see Sec. III) and to check the resolution of the detectors. These sources were made by self-transfer and had therefore negligible thickness. The activity of the sources was 4×10^4 spontaneous fissions per minute, and at least 20 000 events were accumulated in a calibration spectrum.

The calibration of the time scale was achieved by time calibration spectra. In an ideal case, the respective spectra (created via a TAC and an ADC) show sharp peaks at equal 10 ns spacings. However, linear interpolation between the first and the last peak leads to deviations of up

to 100 ps. A third order polynomial provides a better description with average deviations of 16 ps for the various peaks, but nonetheless these deviations had to be investigated carefully, because the fragment velocity determination is crucial for this experiment. Please note at this point that all uncertainties quoted in this paper correspond to one standard deviation.

For time intervals which are small compared to the total analyzed range, errors of the time calibration can be considerably reduced with a differential method. By adding a delay cable (1 or 2 m in length) to the STOP branch of the time calibrator circuit (see Fig. 2), all peaks are shifted from their original positions K_i to k_i by the same time interval Δt. With $\overline{k_i}=0.5\,(K_i+k_i)$ and an unnormalized shift $\Delta t'$, the slope is approximated by

$$\frac{dt'}{dk}(\overline{k_i})=\frac{\Delta t'}{k_i-K_i}\ . \tag{6}$$

Fitting of dt'/dk, integrating, and normalizing with the time difference between the first and the last peak yields an improved time calibration. From the fit of dt'/dk a time calibration error of 10 ps can be deduced, which is not correlated for the two fragment directions. The delay time of the additional cables can be measured with an accuracy of 2 to 3 ps. Owing to the distance of the normalizing peaks of 90 ns and an error of 15 ps at this distance, a very small relative time normalization uncertainty of 15 ps/90 ns $=1.6\times10^{-4}$ is obtained.

H. Fragment energy losses in the sample

As the energy loss of the fission fragments in the sample itself is about 2% of their total kinetic energy, it is obvious that this correction must be investigated carefully. In particular, it has to be treated separately for the UO_2 layer and the carbon backing. The total energy loss (UO_2 layer plus C backing) was measured by inserting the ^{235}U sample in a collimated beam of ^{252}Cf fission fragments. Overall six runs were made with and without the ^{235}U sample in position. For the mean light and heavy fragments we found the following energy losses:

$$\Delta E_{\rm tot}^{{\rm Cf},L}=4.21\pm0.10\ {\rm MeV}\ ,$$

$$\Delta E_{\rm tot}^{{\rm Cf},H}=4.13\pm0.10\ {\rm MeV}\ .$$

The energy losses in the carbon backing can be deduced directly from the $(2E,2v)$ measurement as the mean energies of the U fragments in the two flight paths differ by just that energy loss. We find

$$\Delta E_{\rm C}^{{\rm U},L}=1.83\pm0.05\ {\rm MeV}\ ,$$

$$\Delta E_{\rm C}^{{\rm U},H}=1.83\pm0.07\ {\rm MeV}\ .$$

The dependence of the energy loss ΔE on the fragment mass and energy is taken from the literature. For carbon there are various measurements of ΔE with heavy ions[3,4] and with ^{252}Cf fragments.[5,6] For UO_2 this information must be extrapolated from the respective values for UF_4.[7] This is justified because the stopping power does not depend critically on the mass number of the stopping medium.[4,6] Another possibility is the comparison of energy losses for alpha particles and heavy ions.[8] Combining the measured energy losses for mean fragments with the respective mass and energy dependence, one obtains the following expressions:

$$\Delta E_{\rm U}=0.844+0.01508E+0.0006A -0.000046E^2+0.00027EA\ , \tag{7a}$$

$$\Delta E_{\rm C}=0.316+0.01632E+0.0096A -0.000105E^2+0.000086EA\ . \tag{7b}$$

$\Delta E_{\rm U}$, $\Delta E_{\rm C}$, and E are in MeV and A denotes the mass number. As the mass and energy corrections almost compensate each other, the energy losses for mean light and heavy fragments are nearly equal ($\sim$3.9 MeV for ^{235}U fragments). In the subsequent analysis it is sufficient to consider only mean energy losses. On the average the fragments can be treated as if they had come from the midplane of the uranium layer. Their energy losses are then

$$\Delta E_1=\Delta E_{\rm C}+0.5\Delta E_{\rm U},\quad \Delta E_2=0.5\Delta E_{\rm U}\ , \tag{7c}$$

depending on which side of the sample they are detected. The deviations of the energy loss from the mean value which are caused by the finite thickness of the uranium layer are practically equal and anticorrelated for fragment pairs. Assuming a constant specific energy loss within the sample, the corresponding energy deviations are

$$\sigma_{E_1}=\sigma_{E_2}=\Delta E_{\rm U}/\sqrt{12}\ . \tag{8}$$

Because it depends weakly on E and A, the mean energy loss can be converted from ^{252}Cf fragments to those from ^{235}U with an error of only $\sim$50 keV. In this way an uncertainty of 0.11 MeV is estimated for the mean total energy loss of U fragments in the sample.

I. Measurements

In the preceding we have pointed out that great care was devoted to maintaining an extreme stability for all parameters of the experiment throughout the 1.5 months of operation. In addition, average current, energy, and time structure of the accelerator beam were controlled automatically.

Measurements were performed for fragment flight paths of 70, 170, 270, and 375 mm. Accurately calibrated distance pieces guaranteed flight path uncertainties of only 0.05 mm. From the runs at the two short flight paths, which were carried out at least once a day, the time zero of the TOF spectra was determined. To reduce the effect of long term drifts in the electronics, detectors, and the accelerator on the evaluated data, the measurement was subdivided in 38 runs at 70, 19 runs at 170, 14 runs at 270, and 18 runs at 375 mm flight paths. The number of events per flight path were 58 000, 25 000, 17 000, and 21 000 for 0.50 MeV and 32 000, 10 000, 3500, and 4500 for 5.55 MeV neutron energy. In between those runs 38 time calibrations and 38 energy calibrations were carried out.

Examples for the directly measured raw data are given in Fig. 3 for the pulse height distribution and in Fig. 4 for

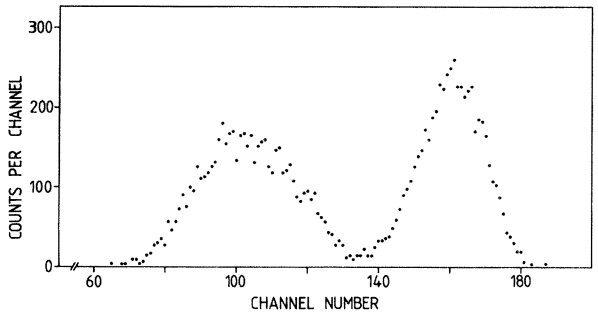

FIG. 3. The experimental pulse height spectrum obtained at 375 mm flight path. The original spectrum of 1024 channels has been compressed to 256 channels for better readability.

the TOF spectra at the various flight paths. For better readability the original resolution had been changed by summation over four neighboring channels.

III. DATA ANALYSIS

A. Survey

Data analysis ($2E,2v$ method) was based on Eqs. (1)—(5). Using nucleon numbers instead of nuclear masses and MeV and cm/ns for energies and velocities, a factor $f=1.930$ must be introduced in Eq. (2):

$$E^*_{1,2}=\frac{A^*_{1,2}}{f}v^{*2}_{1,2} \ . \tag{2a}$$

The analogous expression for the kinetic energies after neutron emission is

$$E_{1,2}=\frac{A_{1,2}}{f}v^2_{1,2} \ . \tag{2b}$$

The fragment velocity is derived from

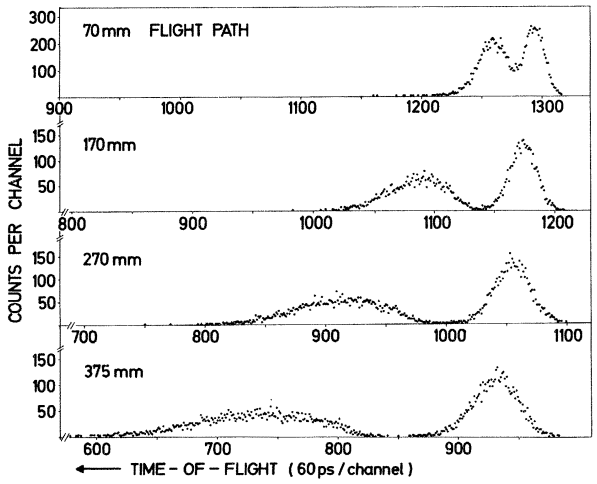

FIG. 4. Time-of-flight spectra taken at various flight paths. The spectra are compressed by a factor 4 to improve the readability.

$$v=\frac{s}{t-t_0} \ . \tag{9}$$

Here, t is the measured flight time for the detector at position s, and t_0 is extrapolated (see below) from the measurements at short flight paths as a function of E and A. Fortunately, this dependence is weak enough so that t_0 is insensitive to the respective uncertainties. From the fragment velocities obtained at long flight paths the primary masses $A^*_{1,2}$ and kinetic energies $E^*_{1,2}$ are calculated from Eqs. (1) and (2a).

The kinetic energies after neutron emission are obtained from the pulse height information PH and a corresponding mass correction according to Schmitt *et al.*[9]

$$E=(a+a'A)\mathrm{PH}+(b+b'A) \ . \tag{10}$$

The constants, a, a' and b, b' can be determined from the ^{252}Cf spectra (Ref. 9). From Eqs. (2b) and (10) E and A can be determined from v and PH. Then the number of emitted neutrons per fragment can be derived from the difference of primary and secondary masses. As t_0 depends only weakly on E and A, a single iteration of this analysis gives consistent data.

In the course of the data analysis we found that the energy calibration scheme of Schmitt apparently yields average secondary masses $A_{1,2}$ which are too large as compared to radiochemical measurements and consequently $\bar{\nu}$ values which are too low, around zero. Therefore, in turn, the constants in the pulse-height—energy relation of Eq. (10) were corrected by comparing the masses $A_{1,2}$ from our analysis with radiochemical masses. This procedure is discussed at the end of this section.

B. Determination of time zero

The time information derived from the surface barrier detectors depends on the pulse shape, and therefore the origin of time scale, t_0, must be determined as a function of E and A. This relation was obtained by analyzing the runs at short flight paths with the ($2E$) method as follows:

$$A^*_1=A_c\frac{E^*_2}{E^*_{K,\mathrm{tot}}} \quad \text{with } E^*_{k,\mathrm{tot}}=E^*_1+E^*_2 \ . \tag{11}$$

Because we approximate $v_{1,2}=v^*_{1,2}$, it is possible to determine the primary energies $E^*_{1,2}$ from the secondary ones by applying a correction for the evaporated neutrons:

$$E^*_i=E_i\frac{A^*_i}{A_i}, \quad A_i=A^*_i-\bar{\nu}(A^*_i,E^*_{K,\mathrm{tot}}) \tag{12}$$

and

$$\bar{\nu}(A^*_i,E^*_{K,\mathrm{tot}})=\bar{\nu}(A^*_i)+C[E^*_{K,\mathrm{tot}}-\overline{E^*_{K,\mathrm{tot}}}(A^*_i)] \tag{13}$$

assuming

$$C=\frac{1}{2}\left\langle\frac{\partial\nu_T}{\partial E_{K\mathrm{tot}}}(A^*_i)\right\rangle \quad \text{with } \nu_T=\sum\nu_i \ .$$

In this way it is possible to calculate the velocity v from E and A. According to Eq. (10) the energy E depends slightly on fragment mass. *Therefore,* with three iteration steps a consistent solution is achieved.

The resulting t_0 values are fitted with a second order polynomial in E and A where $t_0 = t_0(E,A)$ describes the specific timing properties of the detectors (e.g., plasma effects; see Refs. 10 and 11) as well as those of the constant fraction discriminators (CFD's). In the latter case one finds the so-called antiwalk which was investigated by Henschel and Schmidt.[12] By this effect low energy fragments are registered more rapidly than those with high energy. Furthermore, in accordance with pulse shape analyses of Hering and Müller,[13] t_0 is much more dependent on fragment energy than on fragment mass.

C. Corrections for neutron momentum and fragment energy loss

Two additional corrections have to be considered in the above analysis: The momentum of the incoming neutron is transferred to the fragments as momentum in the center of mass (c.m.) system. As the angle θ between the incoming neutron and the fragment direction is 45 deg, the momentum component in the fragment direction accelerates fragment 1, whereas fragment 2 is slowed down. The effect on the kinetic energies is given by

$$E_1^{*\prime} = E_1^* + 2\frac{\sqrt{A_1^* A_n}}{A_c}\sqrt{E_1^* E_n \cos\theta} + \frac{A_1^* A_n E_n}{A_c^2} \quad . \quad (14)$$

For neutron energies of 0.50 MeV one obtains an energy correction of 0.42 MeV for the mean light and heavy fragments. As the signs of these corrections are opposite, there is no change in the total kinetic energy $E^*_{K,\mathrm{tot}}$. The momentum component perpendicular to the fragment direction results in a deviation from fragment colinearity by an angle $\Delta\phi = 0.6$ deg at 0.50 MeV neutron energy and 1.8 deg at 5.55 MeV, and was compensated by bending one of the fragment flight tubes.

After neutron evaporation, which on the average does not change their velocities, the fragments suffer an energy loss ΔE_i in the sample [Eqs. (7a) and (7b)]. This reduces their energies from E_i to $\hat{E}_i$ and their velocities from v_i to $\hat{v}_i$,

$$v_i = v_i' (\hat{E}_i / E_i')^{1/2} \quad \text{with } \hat{E}_i = E_i' - \Delta E_i(A_i, E_i') \quad , \quad (15)$$

which then are measured in the detectors. It is to be noted that the secondary mass can directly be deduced from $\hat{v}_i$ and $\hat{E}_i$.

D. Data selection

The distributions of fragment properties can be severely disturbed by background events, especially in regions where only a few events are observed, e.g., for symmetric fission. It was already described that backgrounds from fragment scattering, spurious pulses, or scattering of the incoming neutrons in the vicinity of the target were suppressed to a large extent. However, the latter problem cannot be eliminated completely, so that single events are recorded which are induced by scattered neutrons, and therefore are considerably delayed with respect to the origin of time.

By proper data selection it is possible to eliminate these bad events without changing the ensemble of genuine events. For the runs taken with short flight paths the origin of time was calculated for all events and both fragments. The deviation δt_1 and δt_2 to the fitted polynomial for average flight times $t(E,A)$ are combined to

$$\delta t_\pm = \delta t_1 \pm \delta t_2 \quad . \quad (16)$$

From the rms width of these quantities, σ_+ and σ_-, one finds that σ_+ is significantly larger than σ_- because of the delayed events associated with scattered neutrons. Only 2% of all events lie outside the 4σ range ($|\delta t_+| > 4\sigma_+$ and/or $|\delta t_-| > 4\sigma_-$) and were eliminated in further analysis.

In the runs at long flight paths data selection was performed analogously, except that in this case the sensitive quantity is the number of emitted neutrons. For each event the calculated neutron number is compared to $\bar{\nu}(A^*, E^*_{K,\mathrm{tot}})$. If the single values deviate by more than four times the rms width, the event is rejected. Again, this holds for only 2% of all cases. It has been shown that within statistics the pulse height distribution of the rejected events was identical to that of the accepted events.

E. Data reduction

For each single run and for light and heavy fragments separately we calculated mean values, rms widths σ, and correlation coefficients r of all relevant observables. Differences in the results obtained in different runs check the stability and are important for the determination of uncertainties. Besides the mean values the distributions of fragment properties are of particular interest.

The following operations were carried out by a single computer program which required the raw data and the calibration measurements as input. It was decided to forego the use of large arrays or extensive intermediate storage of data, because there were many runs to handle and because various iterations had to be carried out during analysis which in turn influenced the input data [corrections of the energy calibration, $\bar{\nu}(A^*, E^*_{K,\mathrm{tot}})$]. At large flight paths (270 and 375 mm), mean values, variances, and covariances of the primary data v^*, A^*, E^*, of the secondary data E, A, and of the number of neutrons ν as well were calculated by the $(2E,2v)$ method. As a check, $E^*_{K,\mathrm{tot}}$ was determined by the $(2E)$ method, too. Associated with the variances σ^2 and the covariances C are the mean slopes of the distributions,

$$\left\langle \frac{dy}{dx} \right\rangle = \frac{C_{xy}}{\sigma_x^2} \quad , \quad (17)$$

e.g., for

$$\left\langle \frac{\Delta\nu}{\Delta A^*} \right\rangle = \left\langle \frac{\Delta(A^* - A)}{\Delta A^*} \right\rangle = 1 - \frac{C_{A^*A}}{\sigma^2_{A^*}} \quad , \quad (17a)$$

where for variables taking only discrete values the derivative is replaced by the quotient of differences. The conditional variances

$$\sigma_y^2(x)=\sigma_y^2\left[1-\frac{C_{xy}}{\sigma_x\sigma_y}\right] \tag{18}$$

e.g., $\sigma_{E^*_{K,\mathrm{tot}}}(A^*)$, and the conditional slopes

$$\left\langle\frac{\partial z}{\partial y}(x)\right\rangle$$

are important in the special case

$$\left\langle\frac{\Delta\nu_T}{\Delta E^*_{K,\mathrm{tot}}}(A^*)\right\rangle=\left\langle\frac{\Delta\nu_T}{\Delta E^*_{K,\mathrm{tot}}}\right\rangle\frac{\sigma^2_{E_{K,\mathrm{tot}}}}{\sigma^2_{E^*_{K,\mathrm{tot}}}(A^*)}$$

$$-\left\langle\frac{\Delta\nu_T}{\Delta A^*}\right\rangle\left\langle\frac{\Delta E^*_{K,\mathrm{tot}}}{\Delta A^*}\right\rangle\frac{\sigma^2_{A^*}}{\sigma^2_{E^*_{K,\mathrm{tot}}}(A^*)}\ . \tag{19}$$

The program calculates the distributions $P(A^*)$, $P(\upsilon^*)$, and $P(A^*_H, E^*_{K,\mathrm{tot}})$ and also the functions $E^*_{K,\mathrm{tot}}(A^*_H)$, $\sigma_{E_{K,\mathrm{tot}}}(A^*_H)$, $\nu(A^*)$, and $\sigma_\nu(A^*)$. The results of the long flight paths are combined, but only half weight was given to the data obtained at 270 mm.

At short flight paths (70 and 170 mm) the kinetic energies were used to determine the time zero function $t_0(E,A)$. As a check, also mean values of primary and secondary quantities as well as the distributions $P(A^*)$ and $P(A^*, E^*_{K,\mathrm{tot}})$ and the functions $E^*_{K,\mathrm{tot}}(A^*_H)$ and $\sigma_{E_{K,\mathrm{tot}}}(A^*_H)$ were calculated.

The expressions t_{0i} which were required for analysis of the long flight path data are weighted averages where a four times larger weight was given to runs at 70 mm than to those at 170 mm.

Statistical uncertainties are directly calculated from the deviations of the various mean values. This means that any stability fluctuations are included in the quoted statistical uncertainties. In the absence of stability problems the uncertainity of the mean values would be

$$\sigma_{\bar{x}}=\sigma_x/\sqrt{N} \tag{20}$$

with N being the number of events. Similar expressions would result for variances and slopes. Stability fluctuations which are independent of N are accounted for by an additional component σ_0

$$\sigma_{\bar{x}_i}=\left[\frac{\sigma^2}{N_i}+\sigma_0^2\right]^{1/2}\ . \tag{21}$$

The stability fluctuation σ_0 is determined such that χ^2 agrees with the number of degrees of freedom f.

One finds from this analysis that correlated variations of t_0 cause the most severe stability problems for the determination of $E^*_{K,\mathrm{tot}}$ and ν_T by the $(2E,2\upsilon)$ method, while the determination of A^*_i by the 2υ and of $E^*_{K,\mathrm{tot}}$ by the $2E$ method is independent of stability fluctuations.

F. Correction of the energy calibration

After the analysis was carried through to this point we found a striking discrepancy between the total kinetic energy determined from the fragment velocities (which are based on the very accurate time calibration) and the total kinetic energy calculated from the pulse height information via the Schmitt calibration scheme.[9] The latter yields a value for $E_{K,\mathrm{tot}}$ which is about 2 MeV too high. These large secondary energies lead to an overestimation of the secondary masses A_i and therefore one obtains values which are far too low for the number of evaporated neutrons. For this reason, revising the constants a,a' and b,b' in Eq. (10) is unavoidable. As was mentioned before, this seems justified in view of the uncertainties quoted by Schmitt *et al.*[9] which are of the same size as the discrepancies discovered.

One possible way to modify the energy calibration is offered by accurate radiochemical measurements of secondary mass yields for thermal neutron induced fission.[14] Comparing mean values and rms widths for light and heavy fragments one can derive four conditions that allow one to change the four calibration constants unambiguously.

As primary masses are not affected by the energy calibration, the required change of secondary masses can be transformed to a change in the number of evaporated neutrons,

$$\delta\nu=-\delta A\ . \tag{22}$$

According to Terrell[15] the slope of $\nu(A^*)$ can be written as

$$\left\langle\frac{\Delta\nu}{\Delta A^*}\right\rangle=1-[(\sigma_A^2-\tfrac{1}{2}\sigma^2_{\nu_{iA^*}})/\sigma^2_{A^*}]^{1/2}\ . \tag{23}$$

Because $\sigma^2_{\nu_{iA^*}}$ represents only a small correction (which is estimated to be 0.6 by Terrell) it is possible to calculate $\langle\Delta\nu/\Delta A^*\rangle$. Thus, the mean values $\bar{\nu}_i$ and $\langle\Delta\nu_i/\Delta A^*_i\rangle$ can be determined directly from the mean values and rms widths of the primary masses and from radiochemically measured secondary masses.

These independent mean values allow adjustment of the energy calibration constants for each detector separately. To this end it is convenient to formulate the calibration such that it is invariant under linear transformations

$$E=(K_1+K_2A)q+K_3A+K_4\ , \tag{24}$$

with

$$q=(\mathrm{PH}-P_1)/(P_1-P_2)\ .$$

PH is the measured pulse height, and P_1 and P_2 are the peak positions for the light and heavy fragments in the ^{252}Cf spectrum. Differentiation yields

$$\frac{dE}{dA}=(K_1+K_2A)\frac{dq}{dA}+K_2q+K_3\ . \tag{25}$$

From Eqs. (24) and (25) the mean values $\bar{q_i}$ and $\overline{(dq/dA)_i}$ can be calculated for both the light and heavy fragments of ^{235}U. Then, any change in the calibration constants K_i yields

$$\delta\bar{E_i}=(\delta K_1+\delta K_2\bar{A_i})\bar{q_i}+\delta K_3\bar{A_i}+\delta K_4 \tag{26}$$

and

$$\delta\left[\frac{\bar{dE}}{dA}\right]_i=(\delta K_1+\delta K_2\bar{A_i})\left[\frac{\bar{dq}}{dA}\right]_i+\delta K_2\bar{q_i}+\delta K_3\ . \tag{27}$$

The relation between δE and $\delta\nu$ is obtained from Eqs. (22) and (23):

$$\delta\overline{E_i}=\delta\overline{A_i}\frac{\overline{E_i}}{\overline{A_i}}=-\delta\overline{\nu_i}\frac{\overline{E_i}}{\overline{A_i}}\ , \tag{28}$$

and correspondingly, with minor approximations,

$$\delta\left[\frac{\overline{dE}}{dA}\right]_i=-\delta\left[\frac{\overline{\Delta\nu}}{\Delta A^*}\right]_i\frac{\overline{E_i}}{\overline{A_i}}\ . \tag{29}$$

Inserting Eqs. (28) and (29) in Eqs. (26) and (27) allows for a calculation of the required corrections for the calibration constants. By reanalysis of all runs it was ensured that these modifications indeed yielded the required values of $\overline{\nu}$ and $\Delta\nu/\Delta A$ consistently. The new calibration constants, averaged over the two detectors, are listed in Table I together with the constants of Schmitt *et al.*[9]

The correction of the energy calibration decreases the secondary kinetic energies by a corresponding increase of the pulse height defect. For ^{235}U and ^{252}Cf the changes in $E^*_{K,\mathrm{tot}}$ are 2.24 and 2.66 MeV, respectively. Furthermore, one finds a weaker mass dependence for a given pulse height

$$\frac{\partial E}{\partial A}=K_2q+K_3\ . \tag{30}$$

For ^{252}Cf $\partial E/\partial A$ is reduced from 0.137 to 0.130 for light ($\overline{q_L}=0$) and from 0.100 to 0.088 for heavy ($q_H=-1$) fragments.

The fact that radiochemical results from thermal neutron fission are combined with the present results obtained at 0.50 MeV neutron energy requires a small correction. But as $\overline{\nu_T}$ changes by only 0.06, a linear interpolation is sufficient in view of the experimental uncertainties. For $\langle\Delta\overline{\nu}/\Delta A^*\rangle_i$ even this correction can be neglected.

G. Resolution effects

The influence of experimental resolution on the measured values is complex, resulting not only in an increased variance but also in a modification of indirectly determined quantities such as $\nu(A^*)$.

To illustrate the resolution effect on mean values, Δ is considered as the genuine deviation of an event from the mean and δ as that owing to the resolution. Then both quantities are uncorrelated and the observed variance is composed of these two contributions. For example, the observed variance of the mean primary fragment mass is

$$\sigma'^2_{A^*}=\langle(\Delta A^*+\delta A^*)^2\rangle=\langle\Delta A^{*2}\rangle+\langle\delta A^{*2}\rangle$$
$$=\sigma^2_{A^*}+\langle\delta A^{*2}\rangle\ . \tag{31}$$

It differs from the original variance by the mass resolution.

The complex influence of resolution effects is discussed for the example of the primary fragment mass. In first approximation the broadening of A^* can be deduced from Eq. (1) to be

$$\delta A^*_2=\frac{\overline{A^*_1A^*_2}}{A_c}\left[\frac{\delta v^*_1}{\overline{v^*_1}}-\frac{\delta v^*_2}{\overline{v^*_2}}\right]\ . \tag{32}$$

With $\delta t/\bar{t}=-\delta v^*/\bar{v}^*$, Eq. (32) can be rewritten to show the influence of time resolution

$$\delta A^*_2=\frac{\overline{A^*_1A^*_2}}{A_c}\frac{1}{s}(-\delta t_1\overline{v^*_1}+\delta t_2\overline{v^*_2})\ . \tag{32a}$$

The time resolution δt contains the resolution of each of the two detectors (which are uncorrelated) and also the correlated effect of the time zero signal which marks the origin of the time scale.

In addition, δA^* is also influenced by the fragment energy losses in the sample. $\delta E^*/E^*=2\delta v^*/\overline{v^*}$ leads to

$$\delta A^*_2=\frac{\overline{A^*_1A^*_2}}{A_c}\frac{1}{2}\left[\frac{\delta E^*_1}{\overline{E^*_1}}-\frac{\delta E^*_2}{\overline{E^*_2}}\right]\ . \tag{32b}$$

A third contribution to δA^* comes from the neutron emission itself. If this is assumed to be independent for the two fragments one obtains for isotropic emission (15)

$$\langle\delta A^{*2}\rangle_n=\left[\frac{\overline{A^*_1A^*_2}}{3A_c\overline{E^*_{K,\mathrm{tot}}}}\right]\overline{\nu_TE^{\mathrm{c.m.}}_n}\ . \tag{32c}$$

For easier survey all these contributions to the experimental mass resolution $\langle\delta A^{*2}\rangle$ are listed in Table II. One finds that in the present experiment a resolution (FWHM$=2.35\sqrt{\langle\delta A^{*2}\rangle}$) of 2.1 mass units was achieved. Obviously, neutron emission is the major constituent of resolution broadening, whereas the relatively large width of the time zero distribution plays only a minor role.

TABLE I. Corrected constants for the pulse height calibration of surface barrier detectors and the respective changes in average kinetic energies of fission fragments.

Calibration constants	K_i			
	a	a'	b	b'
Schmitt *et al.* (Ref. 9)	24.0203	0.03574	89.6083	0.1370
Present work	22.5620	0.04241	88.895	0.12997
Respective change in kinetic energy δE (MeV)				
	δE_L	δE_H		
^{235}U	1.30	0.94		
^{252}Cf	1.46	1.20		

TABLE II. Contributions to the mass resolution from various effects. The overall variance of 0.775 corresponds to a resolution of 2.1 at FWHM.

Effect	$\langle\delta_A^2\rangle$	$\langle\delta A_L^*\delta A_L\rangle$	$\langle\delta A_H^*\delta A_H\rangle$
Neutron emission	0.325		
Time resolution			
Detectors	0.094	0.997	−0.997
Time zero	0.185	0.414	0.287
Fragment energy losses in the sample	0.171		
Mass dependence of the energy calibration		0.084	0.088
Total effect	0.775	1.495	−0.622

Contrary to the mass resolution the spread of the total kinetic energy is dominated by experimental effects, especially by the spread to the time zero signal. Therefore it is of advantage to determine $E^*_{K,\mathrm{tot}}$ by the $(2E)$ method for the calculation of distributions like $E^*_{K,\mathrm{tot}}(A^*)$.

Resolution effects also influence the slope $\Delta\nu/\Delta A^*$ because this is determined as the difference between primary and secondary masses. According to Eq. (17a) the slope $\Delta\nu/\Delta A^*$ is affected by the variance $\langle\delta A^{*2}\rangle$ and by the covariance $\langle\delta A^*\delta A\rangle$ (see Table II). As secondary masses are calculated from kinetic energies and velocities after neutron emission and after the energy loss in the sample, these effects do not contribute to the resolution of $A_{1,2}$, and therefore also not to $\langle\delta A^*\delta A\rangle$. For the light fragments the variance and covariance have equal sign and hence mostly compensate each other, while for the heavy fragments one gets an enhancement of the correction:

$$\left\langle\delta\frac{\Delta\nu}{\Delta A^*}\right\rangle_L=-0.025$$

and

$$\left\langle\delta\frac{\Delta\nu}{\Delta A^*}\right\rangle_H=0.044\ .$$

Both these terms give rise to significant corrections of the slope $\Delta\nu/\Delta A^*$.

Besides the more global effects of the experimental resolution on distributions and functions local effects are also of interest, in particular with respect to the fine structure of the distributions. We have corrected for these effects as follows: Let the original distribution be $g(x)$. Folding with the resolution function $v(x)$ (normalized, mean value zero, variance σ_x^2) yields

$$G(x)=\int g(x')v(x-x')dx'\ .$$

By developing to second order one obtains

$$G(x)=g(x)+\frac{1}{2}\frac{d^2g(x)}{dx^2}\sigma_x^2\ .$$

The inverse relation reads

$$g(x)=G(x)-\frac{1}{2}\frac{d^2G(x)}{dx^2}\sigma_x^2\ , \tag{33}$$

and therefore the iterations given by Terrell[15] and Schmitt *et al.*[9] are not required in this approximation.

For resolution corrections on functions like $\nu(A^*)$ or $E^*_{K,\mathrm{tot}}(A^*)$ one has to consider the spread of two-dimensional distributions. Let $f(x,y)$ be such a distribution which by integration over y yields the one-dimensional distribution $g(x)$. After folding with the resolution function $w(x,y)$ it is

$$F(x,y)=\int f(x',y')w(x'-x,y'-y)dx'dy'\ .$$

If the integral is developed around (x,y) and integrated as in the one-dimensional case above, one finds

$$F(x,y)=f(x,y)+\frac{1}{2}\frac{\partial^2f(x,y)}{\partial x^2}\sigma_x^2+\frac{1}{2}\frac{\partial^2f(x,y)}{\partial y^2}\sigma_y^2+\frac{\partial^2f(x,y)}{\partial x\partial y}C_{xy}\ .$$

Of course integration over y again yields $G(x)$. The original function $\bar{y}(x)$ is given by

$$\bar{y}(x)=\int yf(x,y)dy/g(x)\ .$$

For the resolution broadened function

$$\bar{Y}(x)=\int yF(x,y)dy/G(x)\ ,$$

one obtains

$$\bar{Y}(x)=\bar{y}(x)+\left[\sigma_x^2\frac{d\bar{y}}{dx}-C_{xy}\right]\frac{dg/dx}{g}+\tfrac{1}{2}\sigma_x^2\frac{d^2\bar{y}}{dx^2}\ . \tag{34a}$$

Transformed in second order one finds

$$\bar{y}(x)=\bar{Y}(x)-\left[\sigma_x^2\frac{d\bar{Y}}{dx}-C_{xy}\right]\frac{dG}{dx}\frac{1}{G}-\tfrac{1}{2}\sigma_x^2\frac{d^2Y}{dx^2}\ . \tag{34b}$$

It can be seen from this equation that correlations between x and y (expressed by C_{xy}) as well as the curvature $d^2\bar{y}/dx^2$ must be considered in the unfolding of resolution

effects. Figure 5 illustrates the effect of this unfolding procedure for the example of the mass distribution $P(A^*)$ and of the total kinetic energy distribution $E^*_{K,\mathrm{tot}}(A^*)$. For example, the last term in Eq. (34b) which accounts for the curvature causes a significant correction to the $E^*_{K,\mathrm{tot}}$ curve near $A=130$ resulting in a sharper cutoff towards symmetric fission. It also accounts for the enhancement in fine structure of the mass distribution.

In practice it is important to choose the fit interval small enough compared to the width of the resolution broadening so that possible structures are not ignored. But, on the other hand, it should not be too small so that statistical fluctuations are not interpreted as structure. In regions with only moderate statistical accuracy one has therefore to be very careful with the procedure described here. In Fig. 5 the mass distribution was unfolded with a scan pattern of $\Delta A^*=0.5$, because $\Delta A^*=1$ was found to be insufficient.

H. Geometric effects

Some corrections are also required by the geometric arrangement. Firstly, correction has to be made for the difference between the mean flight path and the shortest distance between sample and detectors, which is not negligible because of the rather large solid angle. This effect is stronger at short flight paths and for the noncoincident events than for the coincident ones because of edge effects.

Secondly, the detection of coincident events is hampered by distorted fragment colinearity owing to neutron emission and fragment scattering in the sample. The effect of neutron emission is determined by the number, the c.m. energy, and the angle of the evaporated neutrons. For isotropic emission one gets for the variance σ^2_ϕ of angular spread

$$\sigma^2_\phi=\frac{2}{3}\frac{A_c}{E^*_{K,\mathrm{tot}}A^*_1A^*_2}\overline{\nu_T E^{\mathrm{c.m.}}_{\mathrm{n}}}\ . \tag{35}$$

Accordingly, fragments of a certain mass A^* which emit many neutrons and hence have a small kinetic energy will have a lower probability for coincident detection than comparable fragments which emit fewer neutrons and are more energetic. This effect can influence the distributions of fragment properties and also the respective mean values.

Experimental data on fragment scattering in sample materials are scarce.[16,17] Denninger[17] reports the following angular spreads: carbon: ($\Delta E_{\mathrm{fragment}}=2$ MeV) $\sigma_\phi=0.0040$; gold: ($\Delta E_{\mathrm{fragment}}=7.4$ MeV) $\sigma_\phi=0.0251$; UO_2 on gold: ($\Delta E_{\mathrm{fragment}}=4$ MeV $+4$ MeV) $\sigma_\phi=0.0214$.

These values show that for our samples fragment scattering is mainly caused by the uranium layer whereas the carbon backing is of minor importance. Expanding the variance of the angular spread linearly in the kinetic energy E^* and in A^*, the total angular spread for both fragments is mass independent.

$$\sigma^2_\phi=\sigma^2_{\phi_1}+\sigma^2_{\phi_2}=a_0+a_1(E^*_{K,\mathrm{tot}}-\overline{E^*_{K,\mathrm{tot}}})\ . \tag{36}$$

Fragment scattering is most pronounced at low kinetic energies and decreases with increasing energy (Joy, Ref. 18).

The influence of all these geometric effects on the experimental results was investigated by a Monte Carlo simulation, which took into account the geometric arrangement, the energy distribution of the neutrons from the (p,n) reaction, the emission of neutrons from the fragments, and fragment scattering. For the assumed distribution $P(E^*_{\mathrm{kin}},A^*)$ all relevant mean values, rms widths, correlations, and slopes are calculated for coincident and noncoincident events and also for the various flight paths. One finds that coincident events observed at long flight paths yield mean primary masses A^*_L which are too high by 0.1 mass unit. Shifts in the energy and mass distribution dictated a correction of the average velocity $\overline{v_H}$ of -0.16%, while the respective correction for $\overline{v_L}$ is negligible. For ν and also for the slopes $\Delta\nu/\Delta A^*$ and $\Delta E^*_{K,\mathrm{tot}}/\Delta A^*$ no significant differences are observed.

From experimentally measured coincident events one obtains a 0.25 MeV larger $\overline{E_{K,\mathrm{tot}}}$ at the 375 mm flight path than at the 70 mm. The additional analysis of all noncoincident events yields the coincidence probability. It decreases from 0.58 at $s=70$ mm to 0.53 at 375 mm. This gives directly a measure for the variance of the mean angular spread: $a_0=0.0002$. For $a_1=0$ the Monte Carlo simulation yields a constant shift in $E_{K,\mathrm{tot}}$ of 0.1 MeV. The experimentally observed shift requires therefore $a_1=-0.00005$ (MeV^{-1}). The parameters a_0 and a_1 so determined are in fair agreement with the values from the literature.[16–18]

Hence, neutron emission and fragment scattering lead to corrections of the mean values of fragment properties that are of the order of 0.1%. The distributions, however, are not significantly affected by these corrections.

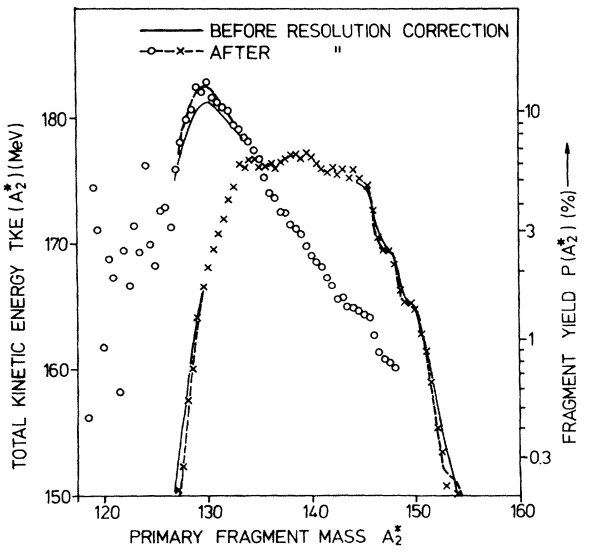

FIG. 5. The correction for experimental resolution results in significant changes in the derived distributions: The maximum in total kinetic energy around $A=132$ is clearly enhanced, while in the mass distribution fine structure shows up in the outer wings.

TABLE III. Summary of the contributions to the systematic uncertainties of the mean primary quantities $\overline{E^*_{K,\mathrm{tot}}}$ and $\overline{A^*_H}$.

Source of uncertainty	$\overline{E^*_{K,\mathrm{tot}}}$ (keV)	$\delta\overline{A^*_H}$
Time calibration $\delta\Delta t = 14$ ps	97	0.033
Flight path dependent distortions $\delta\Delta t = 14$ ps	97	0.033
Flight path differences		
uncorrelated $\delta\Delta s = 0.05$ mm	40	
correlated $\delta\Delta s = 0.05$ mm	56	
Energy loss in the sample		
$\delta E_{\mathrm{tot},L} = 110$ keV		
$\delta E_{\mathrm{tot},H} = 110$ keV	79	0.027
Geometric effects	40	0.02
Normalization of time calibration	57	
Overall systematic uncertainty	186	0.057

I. Flight path dependent distortions

The pulsing system of the accelerator is operated with a frequency of 10 MHz. This could lead to possible distortions of the fast timing signal from the detector which might well be different for different fragment flight paths. The basic frequency of 10 MHz could be eliminated by a high Q filter, but a higher harmonic at 60 MHz could not be suppressed completely, although it was minimized by various groundings.

The remaining high frequency distortions had no influence on the measured fragment velocities, as was verified experimentally by comparing the results obtained at the four flight paths. It was found that the observed deviations of the mean velocities were completely uncorrelated for light and heavy fragments as well as for the two flight directions. The corresponding deviations in time of flight were about 10 ps and are consistent with counting statistics.

In this way, the runs at flight paths of 170 and 270 mm showed that high frequency distortions on the detector signals could be neglected. For further analysis, events from these runs were included with minor weight in the determination of t_0 (170 mm) and of v and ν (270 mm).

J. Summary of systematic uncertainties

This subsection summarizes all systematic uncertainties (one standard deviation). The contribution of these uncertainties to the total error of the two important mean values $\overline{A^*_H}$ and $\overline{E_{K,\mathrm{tot}}}$ will be discussed in detail and listed explicitly in Table III.

At first sight the various uncertainties seem to contribute to the final result in a rather complex way. Fortunately, the situation is considerably simplified by the fact that the primary values $\overline{v^*}$, A^*, and $E^*_{K,\mathrm{tot}}$ which are calculated from the mean flight times of the various flight paths and of both directions agree within their (small) statistical uncertainties with the respective values derived from the complete analysis. Therefore, (i) systematic TOF uncertainties enter only in the TOF difference for the longest and shortest flight path; (ii) uncertainties in the flight path length refer to the difference of 30.5 cm between these flight paths; and (iii) the resulting uncertainties must be averaged, as the fragments move towards both detectors with equal probability.

A contribution to the systematic uncertainty of $\overline{E^*_{K,\mathrm{tot}}}$ is owing to the 10 ps uncertainty in the calibration of the time scale. For the TOF difference this means an uncertainty of 14 ps. Then one finds, according to Eq. (3),

$$\delta E^*_{K,\mathrm{tot}} = \left[\frac{\delta v_1^*}{\overline{v_1^*}} + \frac{\delta v_2^*}{\overline{v_2^*}} \right] \overline{E^*_{K,\mathrm{tot}}} , \tag{37}$$

or in terms of flight time differences,

$$\delta E^*_{K,\mathrm{tot}} = -\left[\frac{\delta t_1}{\overline{\Delta t_1}} + \frac{\delta t_2}{\overline{\Delta t_2}} \right] \overline{E^*_{K,\mathrm{tot}}} . \tag{37a}$$

Averaging over the two directions yields for the light fragments

$$\delta E^*_{K,\mathrm{tot}} = \tfrac{1}{2}[\delta(E^*_{K,\mathrm{tot}})_{L1} + \delta(E^*_{K,\mathrm{tot}})_{L2}]$$

$$= -\frac{\overline{E^*_{K,\mathrm{tot}}}}{2} \left[\frac{\delta t_{1,L}}{\overline{\Delta t_L}} + \frac{\delta t_{2,H}}{\overline{\Delta t_H}} + \frac{\delta t_{1,H}}{\overline{\Delta t_H}} + \frac{\delta t_{2,L}}{\overline{\Delta t_L}} \right] .$$

All flight time differences are statistically independent of each other, and the variance is obtained by quadratic summation

$$\langle \delta(E^*_{K,\mathrm{tot}})^2 \rangle = \left[\frac{\overline{E^*_{K,\mathrm{tot}}}}{2} \right]^2 \left[2 \left[\frac{\delta t}{\overline{\Delta t_H}} \right]^2 + 2 \left[\frac{\delta t}{\overline{\Delta t_L}} \right]^2 \right]$$

$$= (97 \text{ keV})^2 .$$

Another 10 ps time uncertainty was owing to the flight path dependent high frequency distortions from the pulsing system of the accelerator. These result in an equal contribution of 97 keV to the uncertainty of $E^*_{K,\mathrm{tot}}$. The normalization of the time calibration carries an uncertainty of 1.6×10^{-4}, leading to a related uncertainty in $E^*_{K,\mathrm{tot}}$ of 57 keV.

From the measurement of the flight path length one had to consider the uncertainty of 0.05 mm (uncorrelated) as obtained from different readings and a calibration uncertainty of equal size ($\delta s_1 = \delta s_2$, correlated to each other). Their impact on $E^*_{K,\mathrm{tot}}$ is given by

$$\delta E^*_{K,\mathrm{tot}} = \left[\frac{\delta s_1}{\Delta s_1} + \frac{\delta s_2}{\Delta s_2} \right] \overline{E^*_{K,\mathrm{tot}}} . \tag{37b}$$

For $\Delta s_1 = \Delta s_2 = 30.5$ cm one gets a 40 keV contribution to $E^*_{K,\mathrm{tot}}$ from the uncorrelated and a 56 keV contribution from the correlated uncertainties.

A fourth contribution to $\delta E^*_{K,\mathrm{tot}}$ comes from the energy loss in the sample. The error of the total energy loss δE_{tot} (U layer plus C backing) is 110 keV for light and for heavy fragments as well. If the light fragment moves in direction 1, the error is

$$\delta(E^*_{K,\mathrm{tot}})_{L,1} = \delta E_{\mathrm{C},L} + 0.5\delta E_{\mathrm{U},L} + 0.5\delta E_{\mathrm{U},H}$$

and for the opposite direction

$$\delta(E^*_{K,\mathrm{tot}})_{L,2} = \delta E_{\mathrm{C},H} + 0.5\delta E_{\mathrm{U},L} + 0.5\delta E_{\mathrm{U},H} .$$

By averaging one finds

$$\delta E^*_{K,\mathrm{tot}} = 0.5(\delta E_{\mathrm{tot},L} + \delta E_{\mathrm{tot},H}) ,$$

and by quadratic summation

$$\langle \delta(E^*_{K,\mathrm{tot}})^2 \rangle = 0.25(\delta E^2_{\mathrm{tot},L} + \delta E^2_{\mathrm{tot},H}) = (79 \text{ keV})^2 .$$

Finally, geometric effects contribute an additional uncertainty of 40 keV to $\delta E^*_{K,\mathrm{tot}}$. Summation of all these variances leads to an overall systematic uncertainty of 186 keV for the total kinetic energy.

The systematic uncertainty of the primary masses $\overline{A^*_i}$ can be evaluated accordingly, using Eqs. (32), (32a), and (32b). Averaging over the two fragment directions yields the contribution from the time calibration and from the flight path dependent distortions:

$$\delta A^*_H = 0.5(\delta A^*_{H,1} + \delta A^*_{H,2})$$

$$= \frac{\overline{A^*_L A^*_H}}{2A_c} \left[-\frac{\delta t_{L,2}}{\overline{\Delta t_L}} + \frac{\delta t_{H,1}}{\overline{\Delta t_H}} - \frac{\delta t_{L,1}}{\overline{\Delta t_L}} + \frac{\delta t_{H,2}}{\overline{\Delta t_H}} \right] ,$$

and hence

$$\langle \delta A^{*2}_H \rangle = \left[\frac{\overline{A^*_L A^*_H}}{2A_c} \right]^2 \left[2 \left[\frac{\delta t}{\overline{\Delta t_L}} \right]^2 + 2 \left[\frac{\delta t}{\overline{\Delta t_H}} \right]^2 \right]$$

$$= (0.033)^2 .$$

Similarly, uncertainties in flight path length lead to

$$\delta A^*_2 = \frac{\overline{A^*_L A^*_H}}{A_c} \left[\frac{\delta s_1}{\Delta s_1} - \frac{\delta s_2}{\Delta s_2} \right] .$$

For $\Delta s_1 = \Delta s_2$ the contributions from heavy fragments moving in opposite directions differ only by their sign and therefore cancel on the average.

Uncertainties from the energy loss in the sample give rise to an uncertainty

$$\langle \delta A^*_H \rangle = \frac{\overline{A^*_L A^*_H}}{4A_c} \left[\frac{\delta E_{\mathrm{tot},L}}{\overline{E^*_L}} - \frac{\delta E_{\mathrm{tot},H}}{\overline{E^*_H}} \right] ,$$

which gives

$$\langle \delta A^{*2}_H \rangle = \left[\frac{\overline{A^*_L A^*_H}}{4A_c} \right]^2 \left[\left[\frac{\delta E_{\mathrm{tot},L}}{\overline{E^*_L}} \right]^2 + \left[\frac{\delta E_{\mathrm{tot},H}}{\overline{E^*_H}} \right]^2 \right]$$

$$= (0.027)^2 .$$

Geometric effects contribute another uncertainty of 0.02. All these uncertainties add up to the overall systematic uncertainty of $\delta A^*_H = 0.057$.

The systematic errors of variances and correlations are given by uncertainties in the resolution corrections. Among the errors discussed above only that owing to geometric effects is of some importance.

IV. RESULTS

A. General remarks

Before discussing our results in detail we would like to summarize those features of the measurement which were essential to achieve the quoted accuracy:

(i) Maintenance of high stability for all relevant parameters throughout the measurement.

(ii) Subdivision of the measurement into 89 runs at four different flight paths and an additional 38 calibration runs to define energy and time scales. This minimized the influence of drifts in electronics, detectors, or in the accelerator. Remaining effects could be determined and corrected directly from the measured mean values.

(iii) Precise time calibration.

(iv) Consistent data analysis including various internal checks, e.g., calculation of mean fragment velocities (and hence also of primary masses and energies) from the difference of the mean flight times for short and long

TABLE IV. Mean values of fission fragment properties in fast neutron induced fission of ^{235}U. For each result the respective statistical uncertainty is given. Total uncertainties are included in parentheses. For comparison the corresponding quantities for thermal neutron induced fission are included.

		Thermal neutron induced fission			Fast neutron induced fission	
		Milton and Fraser	Hering	Andritsopoulos	This work $(2E,2\nu)$	
Mean values		(2ν)	$(2E,1\nu)$	$(2E,2\nu)$	$E_n=0.50\pm0.08$ (MeV)	$E_n=5.55\pm0.25$ (MeV)
Primary fragment mass	A_L^*	96.08±0.10	96.4	95.87±0.07	96.44±0.03 (0.07)	97.11±0.09
	σ_A^*	5.77		6.3	5.49±0.02 (±0.05)	6.37±0.06
Secondary fragment mass	A_L			94.71±0.06	95.00±0.05[a]	95.63±0.10
	σ_{A_L}				5.332±0.025	6.14±0.07
	A_H			138.60±0.06	138.54±0.05	137.18±0.11
	σ_{A_H}				5.115±0.025[a]	5.96±0.07
Fragment velocities (cm/ns)	v_L	1.409	1.4223	1.415	1.4201±0.0007 (±0.0012)	1.4089±0.0011
	v_H	0.966	0.9824	0.97	0.9813±0.0007 (±0.0010)	0.9856±0.0014
	σ_{v_L}	0.062	0.0522	0.051	0.0518±0.0004 (±0.0005)	0.0676±0.0009
	σ_{v_H}	0.071	0.0691	0.086	0.0698±0.0003 (±0.0005)	0.0740±0.0006
	$r_{v_L v_H}$				−0.561±0.006 (±0.008)	−0.622±0.009
Total kinetic energy (MeV)	$E^*_{K,\mathrm{tot}}$	168.3±1.7	170.6±0.3	167.45±0.2		
	$E^*_{K,\mathrm{tot}}$ (2ν)				170.40±0.15 (±0.25)	169.55±0.22
	$E^*_{K,\mathrm{tot}}$ $(2E)$				170.35±0.05[b]	169.42±0.07[b]
	$\sigma_{E^*_{K,\mathrm{tot}}}$	11.4		14.2	10.05±0.03 (±0.05)	9.98±0.03
	$\langle \sigma_{E^*_{K,\mathrm{tot}}};A \rangle$				7.60±0.03 (±0.06)	8.57±0.04
	$\langle \Delta E^*_{K,\mathrm{tot}}/\Delta A^* \rangle$				1.20±0.01 (±0.03)	0.80±0.02
Number of neutrons per fragment	ν_L	1.19		1.16±0.09	1.44±0.08[a]	1.48±0.05
	ν_H	1.23		1.27±0.09	1.02±0.08[a]	1.71±0.07
	$\Delta\nu_L/\Delta A^*$	0.10			0.039±0.006[a]	0.046±0.006
	$\Delta\nu_H/\Delta A^*$	0.11			0.079±0.006[a]	0.074±0.006
	$\langle(\partial\nu_T/\partial E_{K,\mathrm{tot}})(A^*)\rangle$				−0.131±0.01 (±0.015)	−0.135±0.010
Peak to valley ratio in $P(A^*)$	P/V		500		450±70	30±2
Gradients with excitation energy	$\Delta A_L^*/\Delta E_n$				0.131±0.018 (MeV^{-1})	
	$\Delta E^*_{K,\mathrm{tot}}/\Delta E_n$				−0.180±0.006	
	$\Delta\nu_L/\Delta E_n$				0.010±0.02 (MeV^{-1})	
	$\Delta\nu_H/\Delta E_n$				0.14±0.02 (MeV^{-1})	
	$\Delta(\Delta\nu_L/\Delta A^*)/\Delta E_n$				0.0014±0.0016 (MeV^{-1})	
	$\Delta(\Delta\nu_H/\Delta A^*)/\Delta E_n$				−0.0010±0.0010 (MeV^{-1})	

[a]Results of this work combined with radiochemical data. The respective uncertainties include this normalization uncertainty.
[b]Adjusted to $E^*_{K,\mathrm{tot}}$ (2ν) via energy calibration scheme.

flight paths. Comparison with $E^*_{K,\mathrm{tot}}$ values derived by the $2E$ method revealed significant uncertainties in the usual calibration procedure. Improvements in this point were achieved by inclusion of radiochemical data.

(v) Corrections to the measured data were based on experimental results: fragment energy losses in the sample (directly measured), n emission and fragment scattering (comparison of A^* and $E^*_{K,\mathrm{tot}}$ values obtained with the $2E$ method of various flight paths, comparison of mean values from coincident and noncoincident events) and high frequency distortions from the accelerator (comparison of mean values derived at different flight paths). The consideration of resolution effects is especially important with respect to variances and slopes.

The results presented for $E_n = 0.50$ and 5.55 MeV are various mean values, variances, slopes, and correlations including statistical and total errors. Probability distributions are given for the primary mass and the total kinetic energy. The total kinetic energy, its variance, and the neutron number as a function of the primary mass are shown as graphs. Detailed numerical values are quoted in Ref. 19.

B. Mean values

The mean values of fragment properties and the related variances are important parameters which allow for a systematic comparison between data taken at different excitation energies and with different techniques. In Table IV the mean values derived in this experiment are listed for both neutron energies of 0.50 and 5.55 MeV together with results of Milton and Fraser[20] ($2v$ experiment), Hering[21] ($2E,1v$), and Andritsopoulos[1] ($2E,2v$), which were all carried out with thermal neutrons. For comparison of the results at 0.50 and 5.55 MeV mainly the quoted statistical uncertainties are of relevance. The total uncertainties are included in parentheses. It should be noted that the uncertainties of our mean values are only $\sim 0.1\%$. This ensures that even small differences of these numbers, e.g., $\overline{\nu_i}$, and also the slopes $\Delta\nu/\Delta A^*$ represent relevant results.

Our mean values for the two neutron energies (which correspond to saddle point excitations of 1.3 and 6.3 MeV) differ most significantly for the number of neutrons emitted by the heavy fragments. While $\overline{\nu_L}$ does not change within the quoted uncertainty, $\overline{\nu_H}$ increases by 70%. As other quantities of Table IV do not change considerably with neutron energy, this observation suggests that most of the additional energy is consumed in heavy fragment excitation. There seems to be no easy explanation for this behavior (see Sec. V). Overall, to a good approximation, neutron emission accounts for all the additional excitation energy. It is interesting to note that the mean slopes $\Delta\nu/\Delta A^*$ are independent of excitation energy so that the only change at high excitations is a parallel displacement of the $\nu(A^*)$ curve for heavy fragments.

The extent to which the mass distribution becomes more symmetric with excitation energy can be seen from the decrease in the peak-to-valley ratio. The average total kinetic energy decreases by 1 MeV for the higher neutron energy. All variances increase slightly with excitation. In addition, we find that on the average our variances are smaller than the values from the literature because of our good mass resolution and our corrections applied for resolution effects.

The comparison of our results obtained at 0.5 MeV neutron energy with those for thermal neutron induced fission is complicated by the fact that only Andritsopoulos used a comparable technique and that only Hering applied corrections to the energy calibration scheme of Schmitt. Overall, best agreement is found with the values of Hering, but often the differences compared to the other authors are rather small. Of course, this does not hold for the total kinetic energy, where the results of Milton and Fraser and of Andritsopoulos are certainly too low. These authors also overestimate the related variances $\sigma_{E^*_{K,\mathrm{tot}}}$. Another difference in neutron emission between our results and previous work can be seen from Table IV. For 0.50 MeV neutrons we find that the light fragments emit more neutrons than the heavy ones, in agreement with direct measurements,[22,23] while Refs. 1 and 20 quote almost equal values. In contrast to Milton and Fraser,[20] we also confirm the results of direct measurements for the slopes $\Delta\nu/\Delta A^*$. A further aspect has been pointed out by Niefenecker *et al.*,[24] who found that earlier experiments reported unplausible values for the average energy carried away per neutron. Our result for $\Delta\nu_T/\Delta E^*_{K,\mathrm{tot}}$ yields an average neutron separation energy of ~ 6 MeV and is consistent with recent mass tables.

Summarizing the discussion of Table IV, there seems to be no significant difference between fission with thermal or 0.5 MeV neutrons. Even the sensitive peak-to-valley ratio of the mass distribution appears to be constant within the quoted uncertainty. One possible explanation might be that the saddle point excitation with 0.5 MeV neutrons still lies within the energy gap, and hence shell effects are not yet disturbed by quasiparticle excitation.[25]

C. Mass yield and total kinetic energy

Figure 6 shows a contour plot of the heavy fragment yield versus primary fragment mass and total kinetic energy $E^*_{K,\mathrm{tot}}$ for 0.50 MeV neutron energy. As the distribution is symmetric to $A^* = 118$, the corresponding part for the light fragments is skipped. The various contour lines differ by 10% of the maximum yield.

Besides the pronounced correlation between fragment mass and total kinetic energy, one also observes the same distinct separation between light and heavy fragments as for thermal neutron induced fission.[21] Obviously, there is also some structure in the region of maximum yield which depends on both mass and energy.

D. Primary fragment masses

The primary fragment mass yield is obtained from Fig. 6 by summation over all kinetic energies. In Fig. 7 the resulting distribution is shown as a function of heavy fragment mass for both neutron energies. The peak-to-valley ratio in the distribution which is an indicator for mass asymmetry decreases from 450 for $E_n = 0.50$ MeV (which is still compatible with the value for thermal energies; see Table IV) to 30 for $E_n = 5.55$ MeV. At low excitation the

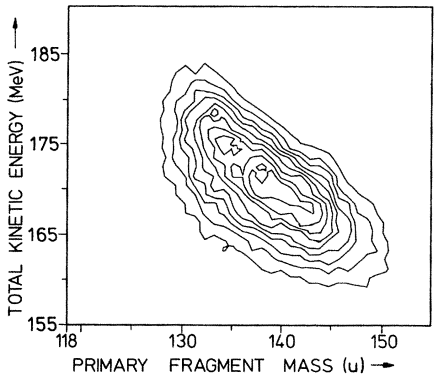

FIG. 6. Contour plot of the fragment yield versus total kinetic energy and primary fragment mass obtained at neutron energies of 0.50 MeV. Contour lines differ by 10% of the maximum yield. The distribution is strongly asymmetric with respect to $A=118$ and shows fine structure at maximum yield.

mass distribution has the shape of a structured plateau with steep wings, whereas at 5.55 MeV neutron energy the wings are flattened and the fine structure is smoothed considerably. It should be noted that the mass resolution does not only allow one to see the fine structure from pairing effects for $A=130$, 135, 140, 146, and 151, but also reproduces the very steep slope of the distribution towards symmetric fission. The structure agrees well with the interpretation of Thomas and Vandenbosch[26] that the maxima correspond to primary fragments with even proton numbers.

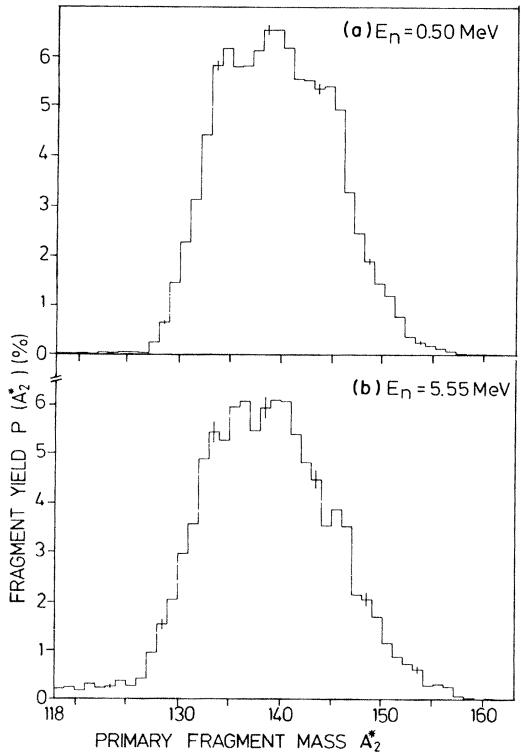

FIG. 7. Primary fragment mass yields $P(A^*)$.

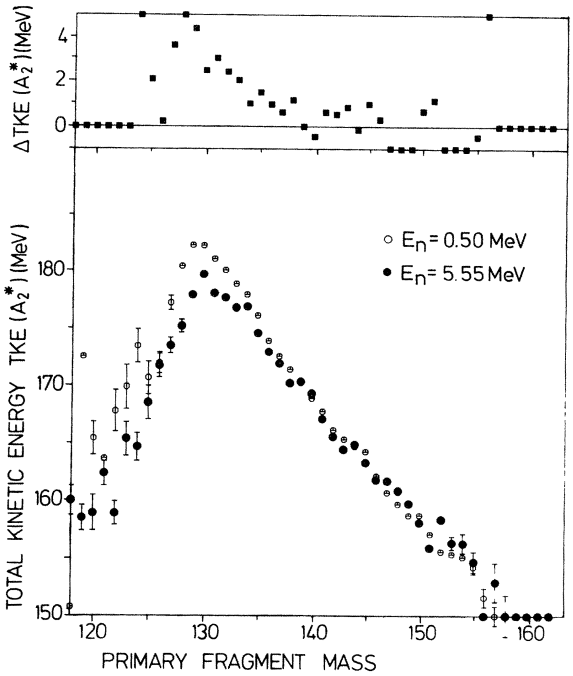

FIG. 8. Distribution of the total kinetic energy $E_{K,\mathrm{tot}}(A^*)$. Error bars are omitted where they exceed 1.5 MeV or where they are smaller than the point size.

E. Total kinetic energy versus primary mass

By far the largest part of the total kinetic energy of the fission fragments is determined by Coulomb repulsion. The observed total kinetic energy is smaller than one would expect if the fragments were created with their ground state deformation.

$$E_{K,\mathrm{tot}} \lesssim E_{\mathrm{Coul}} = \frac{Z_1 Z_2 e^2}{D} \,. \tag{38}$$

This approximation gives an estimate for the minimum fragment deformation at the scission point. Figure 8 shows the total kinetic energy for the two neutron energies. In the upper part of the figure the difference between the two distributions is given separately. The error bars represent the statistical uncertainties which are calculated from the observed variance $\sigma_{E^*_{K,\mathrm{tot}}}$ and the number of events according to Eq. (20). For better readability error bars are shown only if the uncertainty is less than 1.5 MeV.

A significant feature of Fig. 8 is this strong decrease of the total kinetic energy for symmetric fission which clearly points to large fragment deformations. It affects the total kinetic energy by ~20 MeV. Shell effects of only a few MeV cause this decrease and a corresponding increase of the fragment deformation energy. The rapid change of the kinetic energy as a function of fragment mass is correlated with a large value of the variance $\sigma_{E_{K,\mathrm{tot}}A^*}$ (see Sec. V).

The distribution of the total kinetic energy has been investigated also as a function of fragment mass.[27,28] It was

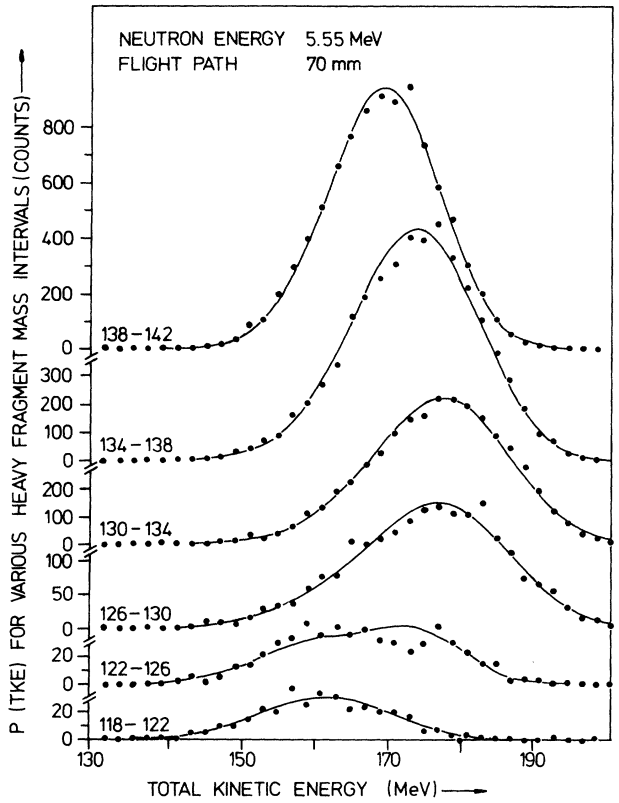

FIG. 9. Distribution of the total kinetic energy $E_{K,\mathrm{tot}}$ for various fragment mass intervals. The solid lines are fits with two Gaussian distributions reflecting a symmetric and an asymmetric mode of fission.

observed that these distributions $P(E_{K,\mathrm{tot}},A^*)$ can be described by superposition of two Gaussian distributions. In Fig. 9 we have shown the situation for the fission of ^{235}U with 5.55 MeV neutrons. For a symmetric mass split one obtains a low energy component $[(E^*_{K,\mathrm{tot}})_1 = 161$ MeV] which is given at the bottom of the figure. A fit of the distributions for an increasingly asymmetric mass split shows that this low energy component is almost independent of fragment mass and that it contributes with equal strength to each mass interval.

With increasing mass asymmetry the contribution of the high energy component increases rapidly, its mean value and width changing with fragment mass. Therefore the mean total kinetic energy can be written as a weighted sum of these two components.

$$\overline{E^*_{K,\mathrm{tot}}(A^*)}$$

$$=[P_1(E^*_{K,\mathrm{tot}})_1+P_2(A^*)(\overline{E^*_{K,\mathrm{tot}}})_2(A^*)]/[P_1+P_2(A^*)] .$$

Obviously, the total kinetic energy is most dependent on A^* for those masses where the two components are comparable. The variance $\sigma_{E^*_{K,\mathrm{tot}}}$ reaches its maximum value for $P_1=P_2(A^*)$. Figure 9 shows that the experimental distributions are well described by the fitted curves.

For 0.50 MeV neutron energy the interpretation of the data near symmetry is impaired by the moderate statistics. Nevertheless, the energy distribution can also be represented by the superposition of two Gaussian functions with about the same mean kinetic energies $(E^*_{K,\mathrm{tot}})_1$ and $(E^*_{K,\mathrm{tot}})_2$ but with very different strengths P_1 and $P_2(A^*)$ compared to $E_n=5.55$ MeV. In this picture, the striking decrease of the $E^*_{K,\mathrm{tot}}$ with increasing excitation energy near $A^*=128$ $(\Delta E^*_{K,\mathrm{tot}}/\Delta E_n=-0.6)$ can be understood by the differences between P_1 and P_2 in the measurements at $E_n=0.5$ and 5.55 MeV.

It can be seen from Fig. 8 that the distribution of total kinetic energy exhibits significant bumps which are clearly correlated with the fine structure in the mass yield. These bumps are present even for the higher neutron energy of 5.55 MeV. It appears plausible that those fragment pairs which are enhanced in yield by shell and pairing effects are also less deformed and hence have a slightly higher kinetic energy of about 0.5 to 1.5 MeV.

Another interesting feature shows up in the variance of the total kinetic energy (see Fig. 10). Obviously, the variance starts with an average value for symmetric fission. Then it rises to a maximum around $A=125$ and drops off until it reaches a constant minimum value at $A=142$. The increase of $\sigma_{E^*_{K,\mathrm{tot}}}$ with excitation is observed for all masses.

F. Neutron emission versus primary mass

While the total kinetic energy gives a measure for fragment deformation at the scission point, the number of prompt emitted neutrons $\nu(A^*)$ provides direct information about the excitation energy of the fragments. Figure 11 shows the typical saw-tooth curve $\nu(A^*)$ for the two neutron energies. The statistical uncertainty is given in those cases where it is less than 0.5 units. At the top of Fig. 11 the difference between the two distributions is given for these significant points. Figure 11 exhibits three important features:

At 0.5 MeV neutron energy there is almost no neutron emission observed from the near doubly magic fragments

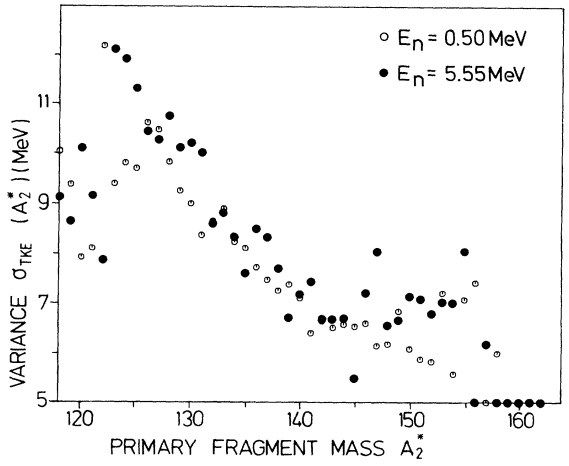

FIG. 10. Variance of the total kinetic energy.

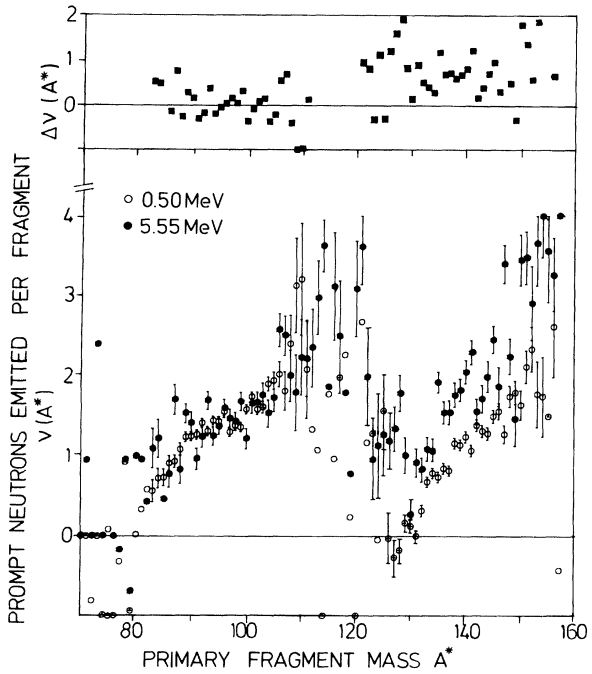

FIG. 11. The average number of neutrons emitted per fragment $\nu(A^*)$. Error bars are omitted where they exceed 50% or a value of 0.5.

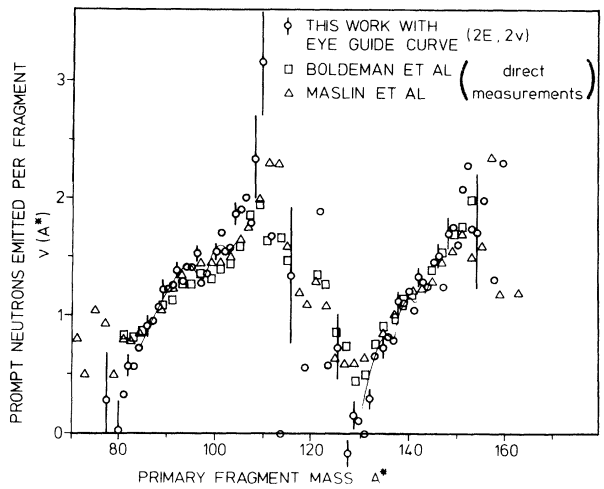

FIG. 12. Comparison of the present results on $\nu(A^*)$ at 0.50 MeV neutron energy with direct measurements at thermal energy using large liquid scintillator tanks. The observed differences may be owing to our better mass resolution. The eye-guide curve through our data indicates fine structure in $\nu(A^*)$.

below $A=132$. Together with the very asymmetric mass distribution this indicates that compared to thermal neutron induced fission, shell and pairing effects are obviously not disturbed by the additional 0.5 MeV excitation energy. With increasing neutron energy fragments with $A=132$ also emit neutrons. But surprisingly, the additional fragment excitation seems to go completely into the heavy fragments without changing the mean slope $\Delta\nu_H/\Delta A^*$. It would be interesting in this context to know whether the variance of $\bar{\nu}(A)$ changes differently with excitation energy for light and heavy fragments. However, such detailed information cannot be obtained by an indirect measurement of neutron emission. There is an indication in the distribution for $E_n=0.5$ that for definite primary masses related to even-proton fragments such as 96/140 and 101/135 the number of neutrons is slightly enhanced for both fragments compared to a smooth $\nu(A^*)$ curve (see the solid line in Fig. 12). Relating ν directly to fragment excitation, this means that the even-proton fragments carry more excitation energy than the average. Because the Q values for these fragments are also somewhat higher than the average owing to ground state pairing corrections, it can be concluded that a considerable amount of the pairing energy is transferred to the excitation energy of the fragments.

G. Comparison with other work

The present work is the first investigation of this kind for fast neutron induced fission, and therefore direct comparison to other work is not possible. But as there are apparently only minor differences between fission with thermal and 0.5 MeV neutrons, Fig. 12 shows the number of prompt fission neutrons emitted per fragment from this work together with the results of two direct measurements which were carried out with large liquid scintillator tanks for neutron detection.[22,23] The present results are shown in steps of 1 mass unit, but in the region of poor statistical accuracy, two or even four points are averaged. The other data exhibit a broader mass resolution because there the fragment masses were measured by the $(2E)$ method and those values are given in steps of 2 mass units.

The overall agreement between the various measurements is remarkably good. The observed differences are consistent with the respective differences in mass resolution. The present data show that the minimum value of $\bar{\nu}$ below the doubly magic fragment with $A^*=132$ in fact is zero. The corresponding light fragments are highly excited and emit up to two neutrons on the average. In addition, a fine structure shows up in the present $\nu(A^*)$ curve which was also found by Milton and Fraser,[29] but not in the direct measurements.[22,23]

V. COMPARISON WITH MODELS OF NUCLEAR FISSION

The scope of fission theory is to evaluate the fission width given by Fermi's golden rule,

$$\Gamma = |\langle f|\hat{H}_{\text{fiss}}|i\rangle|^2\rho(F)\ . \tag{39}$$

The initial state of the target nucleus plus the incoming neutron is denoted by $|i\rangle$, whereas $|f\rangle$ is the final state of two fission fragments in contact. These so-called prompt fragments are subsequently accelerated by their mutual Coulomb repulsion. They dispose of their deformation and excitation energy by emitting neutrons and gamma rays. $\hat{H}_{\text{fiss}}$ is the operator effecting the decay and ρ is the density of states at the excitation energy F in the scission configuration. As mentioned in the Introduction

the fission process passes through a bottleneck, the saddle point, where a maximum amount of energy is in the form of potential energy of deformation. For obtaining the distributions of quantities characteristic of fission, it is sufficient to use the transition states at the saddle point as initial states in Eq. (38). Thus far no microscopic model has been carried through to the comparison with experimental data.

There exists a dynamic classical model for the fission process between saddle and scission.[30] It uses a liquid drop model (LDM) for the potential energy of deformation. The collective kinetic energy is calculated for incompressible, nearly irrotational hydrodynamic flow. The Rayleigh dissipation function describes the transfer of energy of collective motion into internal excitation energy. This model attempts a general description of fragment kinetic energies suppressing quantum mechanical effects.

In statistical models the particular difficulty of fission theory, namely, the calculation of the transition matrix elements in Eq. (38), is circumvented by making hypotheses of a statistical nature. Comprehensive numerical investigations have been performed by Pepping[31] slightly varying the statistical assumptions and using different level density formulae. The fragments were allowed to have quadrupole and hexadecapole deformations. Two prominent results are the following: (i) In order to reproduce the general trend of the experimental data, the distance d between the half-density surfaces of the fragments had to be treated as an adjustable parameter, depending on the mass ratio. The values were in the range $2 \leq d \leq 7$ fm, the larger ones not being understandable in terms of nuclear surface thicknesses. (ii) A constraint had to be introduced to prevent too much energy from leaving the translational degree of freedom, which has a low level density, in favor of the internal degrees of freedom which have a high level density. The conclusions to be drawn from these results are the following: (i) The large values necessary for the parameter d indicate the need for octupole deformations of the fragments. The reduction of the Coulomb repulsion of the fragments thus obtainable would allow one to reduce d. The fact that d has to be a function of the mass ratio probably means that the assumption of a statistical equilibrium is incorrect. (ii) The coupling between the collective degrees of freedom, especially the relative motion of the nascent fragments, to the internal degrees of freedom is so weak that a complete statistical equilibrium is not attained during the fission process.

The model of Wilkins, Steinberg, and Chasman[32] is based on the assumption of a partial statistical equilibrium between the collective degrees of freedom only. Since it yields the best overall agreement between theory and experiment so far, we present the essential features of the model for completeness and compare it with the results of Sec. IV.

The scission configuration is described by two coaxial ellipsoids separated by a distance d. It is further characterized by two temperatures T_{coll} and τ_{int} for the collective and internal degrees of freedom. The values of the three parameters d, T_{coll}, and τ_{int} are approximately constant for all fissioning heavy elements and independent of fragment masses and charges.

By hypothesis fission yields depend only on the density of collective states at the scission point. The energy in these degrees of freedom is given by

$$F = W - V(Z_i, N_i, \beta_i, \tau_{\text{int}}, d), \quad i = 1,2 \; . \tag{40}$$

In this formula the term W represents properties that are independent of a specific fragmentation, like the binding energy of the fissioning nucleus, whereas all terms characterizing the fission fragments are summed up in the term V. These quantities are the deformation energies of the fragments in the scission configuration, their mutual Coulomb repulsion, and final nuclear interactions between the fragment surfaces. The deformation energies include temperature dependent shell and pairing effects obtained from Strutinski's theory. Wilkins *et al.* assume an exponential dependence for the density of collective states as a function of energy: $\rho \sim \exp(F/T_{\text{coll}})$. Since the deformation of the fragments at scission is not measured, and since the relative probability P of different fragmentations is independent of W, one obtains for P

$$P = \int_{\beta_1} \int_{\beta_2} \exp \left| -V(Z_i, N_i, \beta_i, \tau_{\text{int}}, d)/T_{\text{coll}} \right| d\beta_1 d\beta_2 \; . \tag{41}$$

Evaluating this formula numerically Wilkins *et al.* find that neutron shell corrections have a decisive influence on the calculated yields. Proton shell corrections as well as neutron and proton pairing corrections are of minor importance. We present the shell corrections of Ref. 32 in Fig. 13 because they are subsequently referred to.

A. Mass distributions and mass asymmetry

The preference for asymmetric mass division for ^{236}U is easily understood from the behavior of the neutron shell correction. There is no pronounced minimum of the shell correction for symmetric fission ($N = 72;73$), while asym-

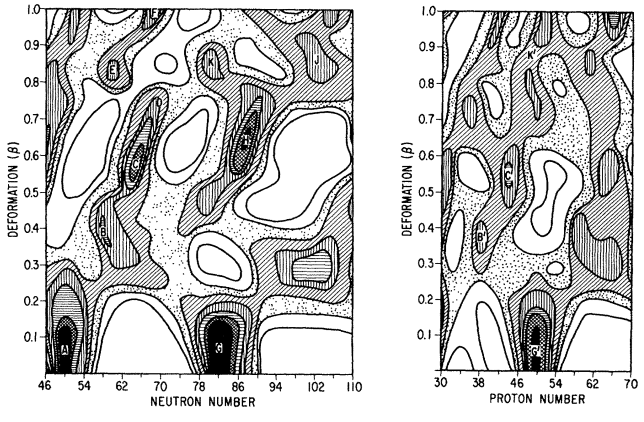

FIG. 13. Shell corrections to the potential energy for neutrons and protons. The figure is taken from the work of Wilkins, Steinberg, and Chasman (Ref. 32). Contours are plotted in intervals of 1 MeV with the black regions containing all values lower than -4 MeV and the inner white regions containing all values greater than $+2$ MeV. The letters refer to particular shell regions as described in the text.

metric pairs have minima at either F and G or at H and C. The LDM energy on which the shell corrections are superimposed favors deformations around $\beta=0.6$; therefore the division H,C is energetically preferred. Consequently, doubly magic fragments near the minima at G and G' with $A\sim 132$ occur relatively seldom. Symmetric fission becomes much more probable when the excitation energy is increased by 5 MeV. In terms of the model the energy increase leads to a stronger coupling between collective and internal degrees of freedom, thus the value of τ_{int} increases and weakens the shell effects. Quantitatively the suppression of symmetric fission is underestimated by the model. Also the calculated width of the mass peaks is too small compared to experimental data. The authors of Ref. 32 suggest that the calculated shell correction in the regions A and B are probably high by 1.5 MeV.

B. Kinetic energy distributions

The model of Wilkins *et al.* qualitatively reproduces the observed total kinetic energy $E_{K,\text{tot}}$ (Fig. 8) and the respective variance $\sigma_{E_{K,\text{tot}}}$ (Fig. 10). The sum of the fragment deformations $\beta=\beta_1+\beta_2$ determines the distance D of the charge centers [Eq. (37)]. In the absence of strong shell effects for symmetric fission, the flat minimum in the potential energy resulting from the LDM terms at deformations $\beta_1\sim\beta_2\sim 0.65$ yields a rather large value for β and consequently for D. Thus the calculated and observed kinetic energies are small. With increasing asymmetry Fig. 13 suggests a very small deformation for the doubly magic fragment $A=132$ at G, while the complementary fragment lies in the region of the minima E and F. The total deformation $\beta\sim 1.0$ is markedly smaller than for symmetric fission and thus $E_{K,\text{tot}}$ rises. For even stronger asymmetry the deformation of the heavy fragments increases to $\beta_2\approx 0.65$ (near point H in Fig. 13), whereas β_1 moves from region C via B towards A. For the respective fragment pairs the sum of deformations lies between 1.2 and 1. Thus the total kinetic energy decreases again. In the region of fragment masses $A>130$ the decrease of the product Z_1Z_2 also reduces $E_{K,\text{tot}}$; this effect is even stronger than the influence of fragment deformation.

The variance of the total kinetic energy shows a significant decrease at $A=140$ (Fig. 10) which is compatible with the Wilkins model. Fragments of mass number $A=138$ and neutron number $N=84$ have complementary fragments with $N=61$. While the deformation of the heavy fragment is fixed by the deep minimum H of Fig. 13, there is no preference for a specific deformation of the light fragment in the relatively broad region between B and C. Hence the variance of the kinetic energy distribution is large. For heavy fragment masses beyond $A=140$ the deformation of the light fragment is confined to the region near B and thus the variance decreases. At present the model cannot discern between prescission and Coulomb contributions to the observed total kinetic energy.

C. The number of prompt fission neutrons as a function of fragment mass

The number of prompt neutrons emitted by a fission fragment is a measure of the sum of deformation energy and prescission excitation energy. The observed saw-tooth structure of the number of neutrons (Figs. 11 and 12) is reflected theoretically in Fig. 13 by lines connecting the minima A,B,C and G,H. Transforming the theoretical deformations to energies of deformation one finds that quantitatively the theoretical saw-tooth curve is too low for the light and too high for the heavy fragments.

Apparently the prediction of the change of $\nu(A^*)$ with excitation energy is beyond the present scope of the model (see Fig. 12 and Table IV). The model predicts a slightly stronger increase of the neutron number for the light fragments than for the heavy fragments because the shell correction minima are less pronounced for the light group. In contrast to this, the experiment shows that the excess in excitation energy goes almost entirely to the heavy fragments. What is therefore needed is an increase of the level density for the heavy fragments. Such a modification would cause a preference for the excitation of the heavy fragments leading to an increase of ν_H and $\Delta\nu_H/\Delta E_{\text{n}}$. If, at the same time, the level density for the light fragments were reduced correspondingly, the calculated gross features of the mass distribution would not be affected.

The conclusion from the comparison of our experimental data to the results of the model is as follows: Even though the accuracy of the calculated terms contributing to the energy V of Eq. (3) is estimated to be 2 MeV and may therefore account for major discrepancies between theory and experiment assuming all theoretical hypotheses to be correct, it seems worthwhile to also consider octupole deformations of the fragments. This degree of freedom allows reducing distance d between the fragments to the range which is physically interpretable in terms of the thickness of nuclear surfaces without increasing the Coulomb repulsion. Even though isolated fragments are stable with respect to octupole deformations, the Coulomb term enforces finite values for β_3 in the scission configuration. For such shapes the shell corrections would exhibit less structure, because of the symmetry-breaking effect of the octupole deformation. In particular the maxima of the shell corrections would be flattened and thus the valleys would be filled up. This would cause a desired broadening of the calculated mass distribution. Strong effects localized in the space of deformation parameters would occur at the crossing of levels which differ in their asymptotic Nilsson quantum numbers by $\Delta N=1$, $\Delta n_Z=1$ if the crossing takes place close to the Fermi surface. Whether these effects would reduce the discrepancies between theory and experiment substantially can, however, be decided only after extending the calculations of Ref. 32.

VI. CONCLUSIONS

A comparison of our results with detailed model calculations confirms the general theoretical concept. However, very specific results such as the mass and energy

dependence of $\nu(A^*)$ indicate that some modifications of the Wilkins *et al.* model are necessary concerning the shell effects of heavy fragments. It appears to us that an additional deformation degree of freedom for the nascent fragments would be appropriate. Unfortunately, the model can also not account for the change of fragment properties within the small but important energy interval from thermal neutron induced fission up to the (n,n*f*) threshold which was covered in our experiment. Finally, we point out that the experimental technique was improved to a point where the resolution is dominated by neutron evaporation effects.

ACKNOWLEDGMENTS

We are very much indebted to Prof. F. Gönnenwein who suggested this experiment and promoted it by stimulating discussions and continuous support. We appreciate the excellent sample preparation at the University of Munich by Dr. H. J. Maier, the careful technical assistance of G. Rupp, and the important contribution of A. Ernst and D. Roller from the Van de Graaff team in providing the computer controlled fast pulsed proton beam. This work was carried out at Kernforschungszentrum Karlsruhe and was in part supported by the Bundesministerium für Forschung und Technologie.

---

*Present address: Siemens AG, D-8000 München, Federal Republic of Germany.

†Present address: Department of Physics, University of Petroleum and Minerals, Dhahran, Saudi-Arabia.

[1]G. Andritsopoulos, Nucl. Phys. A94, 537 (1967).

[2]H. W. Schmitt and F. Pleasonton, Nucl. Instrum. Methods 40, 204 (1966).

[3]H. Pape, H.-G. Clerc, and K.-H. Schmitt, Z. Phys. A 286, 159 (1978).

[4]C. D. Moak and M. D. Brown, Phys. Rev. 149, 244 (1966).

[5]L. Hagel, thesis, University of Tübingen, 1979 (unpublished).

[6]R. Müller and F. Gönnenwein, Nucl. Instrum. Methods 91, 357 (1971).

[7]L. B. Bridwell and C. D. Moak, Phys. Rev. 156, 242 (1967).

[8]J. F. Ziegler, Appl. Phys. Lett. 31, 544 (1977).

[9]H. W. Schmitt, W. M. Gibson, J. H. Neiler, F. J. Walter, and T. D. Thomas, *Proceedings of the Symposium on Physics and Chemistry of Fission, Salzburg* (IAEA, Vienna, 1965), Vol. I, p. 531.

[10]H. Meyer, IEEE Trans. Nucl. Sci. NS-13/3, 80 (1966).

[11]M. Moszynski and B. Bengtson, Nucl. Instrum. Methods 91, 73 (1971).

[12]H. Henschel and R. Schmidt, Nucl. Instrum. Methods 151, 529 (1978).

[13]B. Hering and R. Müller, Nucl. Instrum. Methods 153, 235 (1978).

[14]E. A. C. Crouch, At. Data Nucl. Data Tables 19, 417 (1977).

[15]J. Terrell, Phys. Rev. 127, 880 (1962).

[16]D. Kerr, G. Siegert, K. Kürzinger, E. Konecny, and H. Ewald, Z. Naturforsch. 22a, 1799 (1967).

[17]R. Denninger, thesis, University of Tübingen, 1976 (unpublished).

[18]T. Joy, Nucl. Instrum. Methods 106, 237 (1973).

[19]R. Müller, A. A. Naqvi, F. Käppeler, and Z. Y. Bao, Kernforschungszentrum Karlsruhe Report 3320, 1981.

[20]J. C. D. Milton and J. S. Fraser, Can. J. Phys. 40, 1626 (1962).

[21]B. Hering, thesis, University of Tübingen, 1979.

[22]E. E. Maslin, A. L. Rodgers, and W. G. F. Core, Phys. Rev. 164, 164 (1967).

[23]J. W. Boldeman, A. R. de L. Musgrove, and R. L. Walsh, Aust. J. Phys. 24, 821 (1971).

[24]H. Nifenecker, C. Signarbieux, R. Babinet, and J. Poitou, *Proceedings of the Symposium on Physics and Chemistry of Fission* (IAEA, Vienna, 1974), Vol. II, p. 117.

[25]F. Käppeler and F. Dickmann, in Proceedings of the NEANDC/NEACRP Specialists Meeting on Fast Neutron Fission Cross Sections of U-233, U-235, U-238, and Pu-239, 1976, Argonne National Laboratory edited by W. P. Poenitz and A. B. Smith, Argonne National Laboratory Report ANL-76-90, 1976, p. 391.

[26]T. D. Thomas and R. Vandenbosch, Phys. Rev. 133, B976 (1964).

[27]E. Pfeiffer, Z. Phys. 240, 403 (1970).

[28]W. Holubarsch, thesis, University of Tübingen, 1979.

[29]J. C. D. Milton and J. S. Fraser, *Proceedings of the Symposium on Physics and Chemistry of Fission, Salzburg* (IAEA, Vienna, 1965), Vol. II, p. 39.

[30]K. T. P. Davies, A. J. Sierk, and J. R. Nix, Phys. Rev. C 13, 2385 (1976).

[31]P. Fong, *Statistical Theory of Nuclear Fission* (Gordon and Breach, New York, 1969); R. E. Pepping, Los Alamos National Laboratory Report LA-8047-T, 1979 (unpublished).

[32]B. D. Wilkins, E. P. Steinberg, and R. R. Chasman, Phys. Rev. C 14, 1832 (1976).